SD-TR-80-71

AD A095131

② S

ACTIVE MIRROR HOLOGRAPHIC INTERFEROMETRY

R. R. Shannon and W. S. Smith
Optical Sciences Center
University of Arizona
Tucson, Arizona 85721

LEVEL Ⅱ

1 September 1978

Final Report
Contract F04701-75-C-0106

DTIC
SELECTE
FEB 18 1981

E

Approved for public release;
distribution unlimited

Prepared for
Space and Missile Systems Organization
DYS
Worldway Postal Center
Los Angeles, CA 90009

DDC FILE COPY

81 2 17 113

This final report was submitted by the Optical Sciences Center, University of Arizona, Tucson, Arizona 85721, under contract F04701-75-C-0106 with the USAF Hq Space Division, Los Angeles, CA 90009. This report has been reviewed and cleared for open publication and/or public release by the Public Affairs Office (PAS) in accordance with AFR 190-17 and DODD 5230.9. There is no objection to unlimited distribution of this report to the public at large, or by DTIC to the National Technical Information Service (NTIS).

This technical report has been reviewed and is approved for publication.

GARY M. ROWE, Capt
Project Engineer

JAMES A. JANZEN, Maj
Project Engineer

FOR THE COMMANDER

RICHARD B. KEHL, Col
Director, Space Test Program
Deputy for Technology

SECURITY CLASSIFICATION OF THIS PAGE (When Data Entered)

REPORT DOCUMENTATION PAGE		READ INSTRUCTIONS BEFORE COMPLETING FORM
1. REPORT NUMBER SD-TR-80-71	2. GOVT ACCESSION NO. AD A095131	3. RECIPIENT'S CATALOG NUMBER
4. TITLE (and Subtitle) Active Mirror Holographic Interferometry		5. TYPE OF REPORT & PERIOD COVERED Final report
		6. PERFORMING ORG. REPORT NUMBER
7. AUTHOR(s) R. R. Shannon and W. S. Smith		8. CONTRACT OR GRANT NUMBER(s) F04701-75-C-0106
9. PERFORMING ORGANIZATION NAME AND ADDRESS Optical Sciences Center University of Arizona Tucson, AZ 85721		10. PROGRAM ELEMENT, PROJECT, TASK AREA & WORK UNIT NUMBERS
11. CONTROLLING OFFICE NAME AND ADDRESS SAMSO/DYS P.O. Box 92960 Worldway Postal Center, Los Angeles, CA 90009		12. REPORT DATE September 1978
		13. NUMBER OF PAGES 78
14. MONITORING AGENCY NAME & ADDRESS(if different from Controlling Office)		15. SECURITY CLASS. (of this report) Unclassified
		15a. DECLASSIFICATION/DOWNGRADING SCHEDULE

16. DISTRIBUTION STATEMENT (of this Report)

Approved for public release; distribution unlimited

17. DISTRIBUTION STATEMENT (of the abstract entered in Block 20, If different from Report)

18. SUPPLEMENTARY NOTES

19. KEY WORDS (Continue on reverse side if necessary and identify by block number)

Active optical systems
Holographic interferometry
Large optical components
Astronomical optics

20. ABSTRACT (Continue on reverse side if necessary and identify by block number)
The concept of a completely integrated optical mirror and support structure
for use in large astronomical telescopes was studied. The mirror would have
a complex substructure consisting of an arrangement of double triangular active
supports. These supports would provide stiffness in two directions at 41 sup-
port points. The support points would be modular and be linked together. Two
active optical systems were analyzed: a 33 actuator system and a 41-actuator
system. A 60-cm aperture system was designed and constructed with three active

DD FORM 1473 EDITION OF 1 NOV 65 IS OBSOLETE

INTRODUCTION

The use of large astronomical mirrors in space and on the ground makes complex mechanisms necessary for their support. The magnitude of the support mechanism is generally proportional to some power of the mass of the mirror. Therefore, it is beneficial to reduce the mass of the mirror to be supported to its minimum possible value. In this study a totally new approach is presented for an actuator-controlled primary mirror.

The concept discussed here is that of a completely integrated optical mirror and support. The optical surface is reduced to the essential--a single, thin, membrane-like surface. In order to maintain the membrane action, the diameter-to-thickness ratio of the optical component may be 100:1 or larger. The main purpose of increasing the thickness of the mirror is to increase the stiffness to a level at which the number of support points required may be greatly reduced. In a space application, a membrane may be used more effectively than in a ground-based application. In addition, previous work has shown that a complex structure with a web and connections of the support points to the central plane or surface of the web offer significant advantages in spite of the added complexity and mirror construction.

In short, the concept consists of taking a mirror made from ULE, Cer-Vit, or perhaps fused silica and developing a complex substructure. (The use of a metal substrate has some advantages. As we will see in the experimental work, it does not break during the testing period.) The substructure consists of an arrangement of double triangular active supports. These supports provide stiffness in each of two directions at 41 support points. Relatively simple mechanical actuators are used to drive the apices of the triangles in

1

Z direction and in X and Y tilt directions. Actual position is maintained by application of a force actuator in the direction parallel to the axis of the mirror with tilts in the tangential and radial directions. The position is obtained from lateral forces applied to central portions of each set of modular support components.

A central feature in the concept is that the support points (the individual triangular truss components) are modular and are linked together at a number of positions. The requirement for a stiff backup structure against which forces are applied is eliminated, although that approach was used in a scale model tested in the laboratory.

In a previous report, several proposed techniques for surface sensing and feedback control of the actuators were discussed. The purpose of the study reported here was to examine the mechanical behavior of a scale model of a candidate 3-m-diameter primary mirror. The results were not obtained without some trial (particularly with damage to the rather delicate scaled-down in thickness front plate) but indicate that the concept is a valid one since the results of computer analysis match the experimental results.

An important point about the approach being discussed here is that exotic materials are not intrinsic to the design itself. In fact, calculations on the possible weight saving for mirrors in the 3 to 4-m class indicate that steel tubing for the components, rather than carbon fiber or other exotic material, is sufficient to produce a workable mirror that is 1/20th the weight of a conventional solid mirror. More engineering obviously could reduce this weight even further.

The handling of such a component must necessarily be done as an integrated structure. There are no significant problems in using small-lap,

2

automated polishing techniques for working the surface. Large lateral and radial loads must of necessity be avoided.

The dynamics of the mirror structure were not investigated. However, the design intrinsically involves the use of truss components in a coupled structure in which there are many differing truss lengths. This should distribute any vibratory modes across a broad frequency spectrum. Proper selection of materials and base tension in the components should allow movement of the resonant frequencies to a high region.

In summary, the concept being discussed here and reported on previously appears to be workable and reliable for consideration in future applications of large mirror structures. The concept also allows materials in common use at the present time to be used as structural components for this mirror support.

SCOPE OF WORK

· The statement of work notes that the contractor shall design "a proto-type active mirror which will demonstrate the validity of the active optics concept..." and shall "design in detail and computer analyze an active mirror system, encompassing the primary mirror, actuators, and figure subsystem."

Under the previous contract several concepts of active optical systems were devised and computer analyzed using finite element programs. Particular attention was given to support of the outer edge since this was the source of the majority of the residual figure error in the initial designs.

Two of these systems were analyzed further under this contract: a 33-actuator and a 41-actuator system. The 41-actuator system looked more prom-ising and was chosen for extensive computer analysis. A 60-cm aperture system was designed and constructed with three active and 38 stationary supports. Improved holographic testing was used to demonstrate the control of the optical figure at the three active control points.

DESIGN CONSIDERATIONS

The active mirror systems studies under this contract differ from other concepts in two important respects. First, each mirror actuator controls the surface in three ways: axial or normal position, and slope about two orthogonal axes. Second, the mirror element forms part of the structure instead of being referenced to a much stiffer support. This increases the structural efficiency of the total system.

"The "integrated" active mirror aud support have an increased efficiency since the loads are carried in the direction of maximum stiffness of tensile-membrane action. The weight of the system is minimized when the membrane of the shell (the active mirror) becomes part of the structure.

The number of actuators required for a system is a function of several variables: the mirror stiffness, the scale of the residual errors, the magnitude of the residual errors, and their form.

In choosing the 41-actuator system for further study the effects of "scalloping" have been alleviated by closer placement of actuators at the edge. The scalloping, which was demonstrated early in our active optics studies, is a result of attempts to make slight changes in the basic radius of curvature.

A pure radius change of the shell of the mirror would require a state of stress that had, for its boundary conditions, a uniform radial membrane stress reacted by a uniform pressure applied to the surface of the shell. Bending and shear stresses along the boundary would not exist. In attempting to produce this change through the bending of the shell by a discrete number of actuator points, deflections that are functions of angular position are

obtained. Since the membrane stiffness (the stiffness associated with middle surface stretching) for the mirror is several orders of magnitude larger than the bending stiffness (the stiffness associated with the formation of a "developable" shape), and these are coupled in shell action, the membrane stiffness effect dominates, forcing considerable bending to occur in order to accommodate the enforced displacements at the actuator points. Since the membrane stiffness varies with t, the thickness of the shell, and the bending stiffness with t^3, it is apparent that by increasing the mirror thickness, the scalloping effect may be reduced.

This effect is considerably smaller for an astigmatic and comatic type of surface error as the edge zone is warped (bending action) rather than becoming compressed or extended (membrane action). Thus astigmatic and comatic errors are both easier to correct and more likely to occur for the same reason.

Obviously, the design of an entire system would require a complete parametric study, which was beyond the scope of this program.

The 33-Actuator System

As a result of the study of the 9-actuator system, more advanced configurations were designed. The 33- and 41-actuator systems were studied in depth. The 33-actuator system is illustrated in Figs. 1, 2, and 3. This design was abandoned in favor of the 41-actuator system because of the elongated truss configuration used and the flexibility of the reference structure.
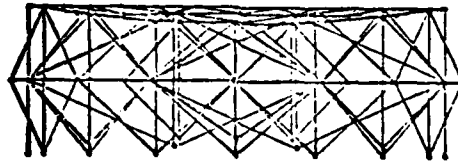
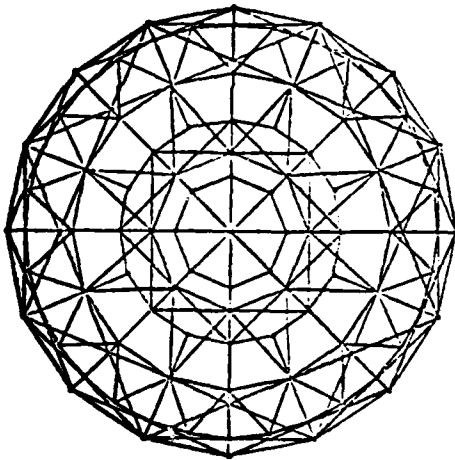Fig. 1.   Elevation view of the 33-
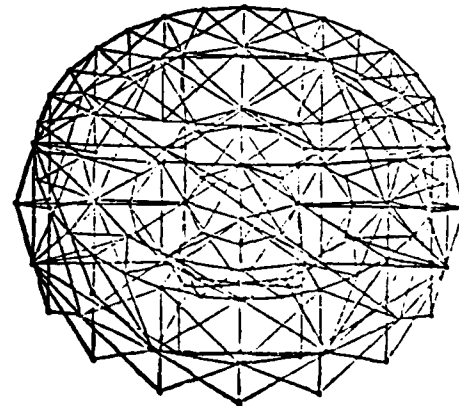actuator system.

Fig. 2.   Plane view of the 33-actuator
system

Fig. 3.   Trimetric view of the 33-
actuator system.

7

The 41-Actuator System

In order to increase the stiffness and structural efficiency of the support structure, the truss and the reference structure are integrated, as illustrated by the truss configuration in Fig. 4. Here the truss is modified to include the additional horizontal reference structure element. The angle of the truss elements is also changed to 45° for the central truss, to maximize truss stiffness. This allows for the elimination of pretension in the truss for large systems where the truss elements are structurally stable.

Radial alignment of the trusses is intrinsic to the system, being a component of a symmetrical optical system. Radial slope control of the mirror's surface can be achieved by the in-plane slope control of the truss. Simultaneously, the stiffness of the reference structure is increased by the spoke configuration created by this radial alignment. Since the spatial frequency of the error can be adjusted by a proper modification of the stiffness of the structure, a minimum spatial frequency of D/5 is assumed. The width of the trusses is reduced to D/5 to increase their stiffness and allow for their radial alignment and localized figure control.

A top view of the support structure is shown in Fig. 5. In this figure, 16 tangentially aligned trusses have been added at the points where scalloping would have maximized in their absence. The positions of the actuators were made four-way symmetric in order to make the width of the edge actuator truss approximately D/5. The central actuator is a three-dimensional truss. Figure 6 is a meridional section view of the structure that illustrates the change in the actuator truss height with radial position and the symmetry of the truss about the reference structure.
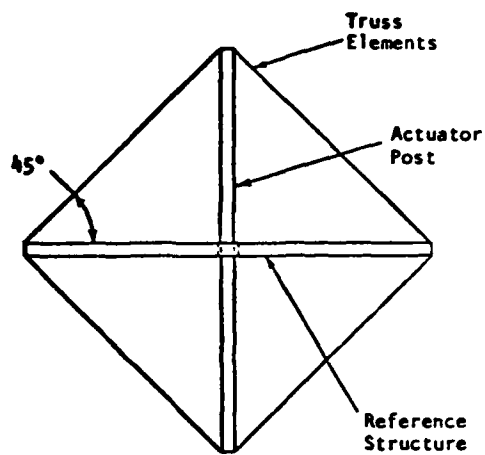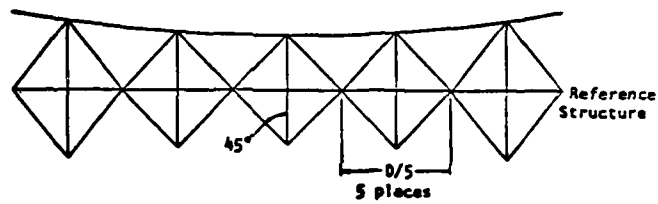
Fig. 4. Modified center actuator configuration.

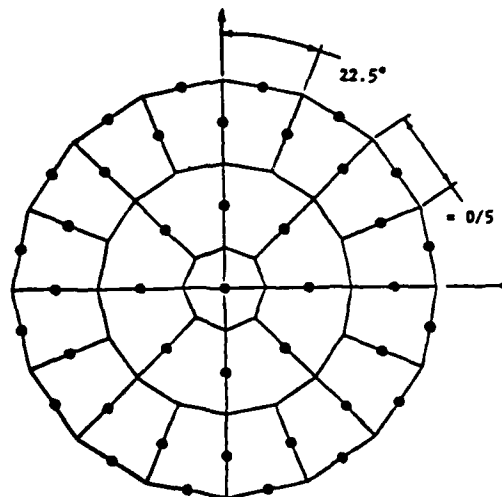Fig. 5. Section view of truss configuration along meridional plane.

Fig. 6. Top view of truss configuration.

9

The Mathematical Model

The mathematical simulation of the prototype consists of a 244-node finite element model illustrated in a top view in Fig. 7, a side view in Fig. 8, and a 30° oblique view in Fig. 9. The geometric configuration of the structure was described previously. One-hundred sixty-eight bar elements (no bending stiffness) represent the 0.81-mm-diameter steel wire truss elements; 198 beam elements are used to model both the 6.8-mm-diameter aluminum actuator posts and the 19.05-mm square aluminum components of the reference plate. The model of the 60-cm-diameter pyrex mirror, having a thickness of 3.18 mm and a radius of curvature of 1.83 m, is composed of 112 plate bending elements. Since the structure is four-way symmetric, the boundary conditions are the three suppressed translational degrees of freedom of the reference plate's four outside nodes along the X and Y axes, as illustrated in Figs. 7 and 8. A section view of the model along the Y axis is shown in Fig. 10. The nodes in the proximity of the intersection between the actuator post and the reference plane coincide.

Slope control in the direction parallel to the plane of the truss is illustrated in Fig. 11. For mechanical simplicity of the prototype, the actuator is bent to produce the angular deflection. The angular deflection of the mirror surface depends upon how much the actuator post is bent and how much the lower truss elements are stretched since movement of the top of the truss is restrained due to the membrane stiffness of the shell coupled with the truss stiffness of the rest of the structure.

Slope control in the direction perpendicular to the plane of the truss is done in the same manner (i.e., force and reaction is between the coincident nodes). The angular displacement for this case will be much larger, for the
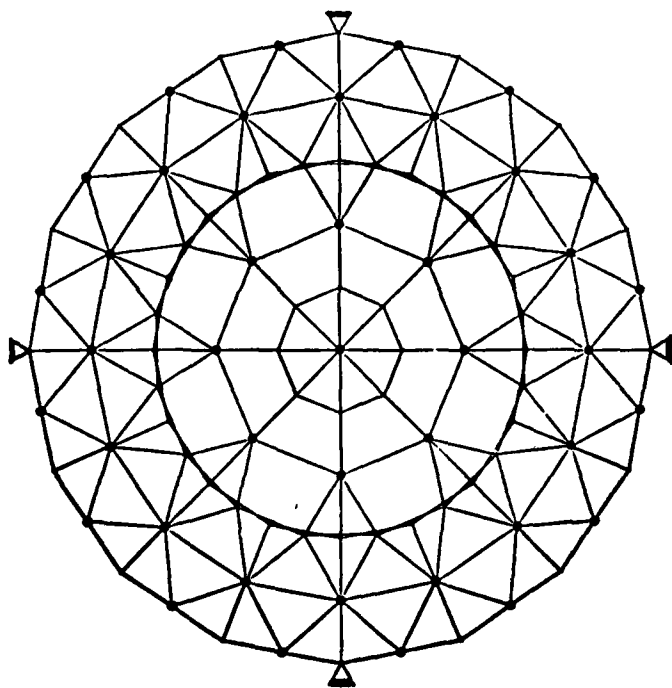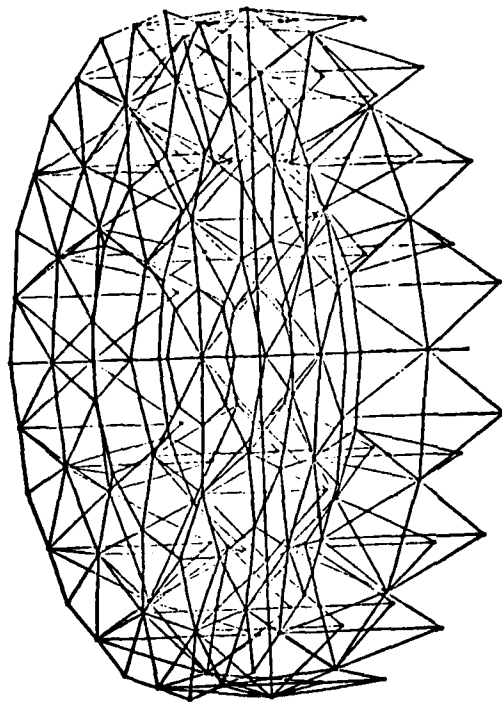
10

Fig. 9. 30° oblique view of the finite element model.

Fig. 10. Section view of the finite element model along the X axis.
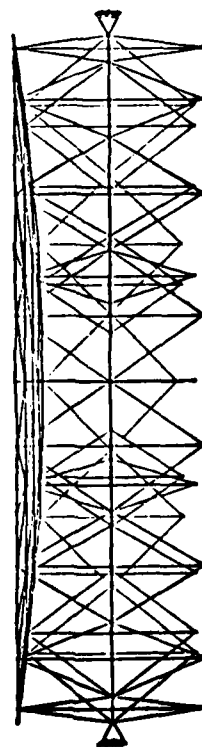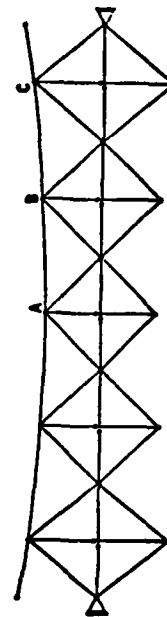

Fig. 7. Top view of the finite element model.

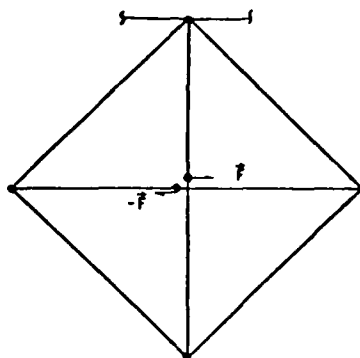Fig. 8. Side view of the finite element model.

11

Fig. 11.   In-plane slope control.

same load, than for the in-plane slope control, since the truss has no stiff-
ness in this direction and the moment created by the forces must be reacted
entirely by the bending stiffness of the shell.

Normal position control of the prototype is most accurately represented
by the modified truss model illustrated in Fig. 12, using the "slave node"
option in SAP IV (Bathe et al., 1973). This option forces a specified
placement of a beam element to be equal to that of the so-called "master node."
Besides requiring these additional nodes, which generally increase the band-
width of the stiffness matrix, this method alters the stiffness of the truss
at the mirror (no stiffness in Z-translation at node "A"). In other words,
this method requires a modification of the model's stiffness matrix before
the equation solution routine begins in the program. Since only the actuator
upon which the normal position loads are applied can be modified, only one
load case of position control can be treated at a time. This greatly in-
creases the cost of the analysis, since the equation solution routine in the
program is the most expensive routine in a static analysis. All slope control
load cases can be handled in a single computer run since the stiffness matrix
is not altered. Normal position control using the unmodified truss is illus-
trated in Fig. 13.

Node "A" is the master node of node "B" in all degrees of freedom except Z translation

Sliding beam element

Node "C" is the master node of node "D" in all degrees of freedom except Z translation
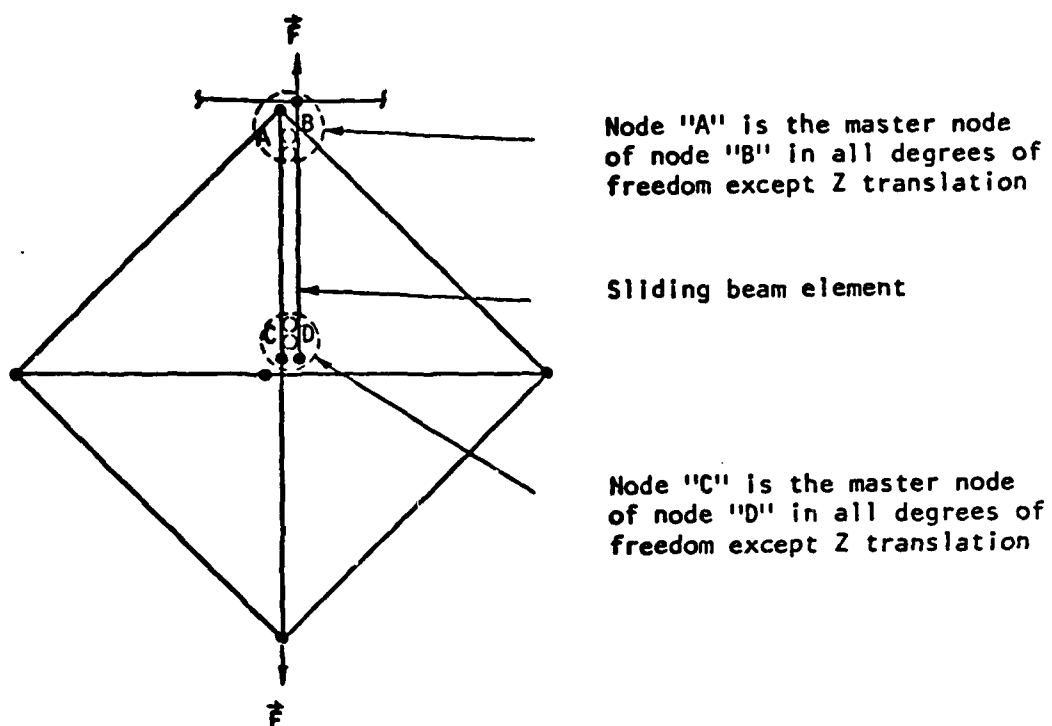
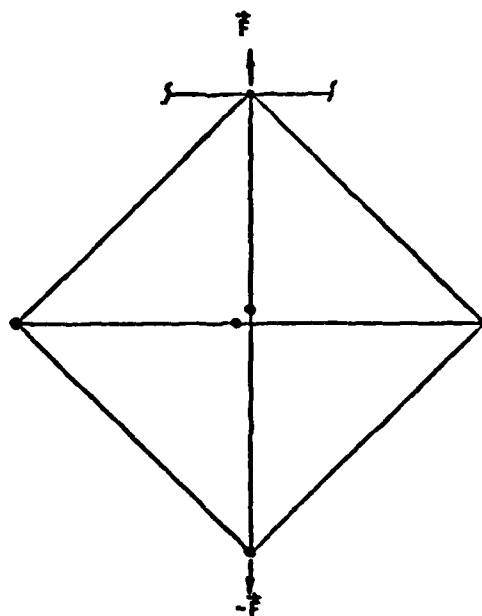Fig. 12.   Ideal normal position control truss model.

Fig. 13.   Normal position control truss model that was used.

Here the loads are applied to the ends of the truss, directly loading not only the shell, but also the truss elements and the actuator post. The results will be the same as the other method but are scaled, since most of the load is reacted by actuator post. The discretized shell of the mirror is illustrated in Fig. 14. The large nodal points in the figure are the locations of the actuator posts. Additional nodal points were necessary to properly model the shell (i.e., geometrically isotropic model) and to provide more data points for interpolation of the data. Close inspection of the figure will reveal the fact that the model is composed of, in part, triangular elements having edges along the circumference of the model that are not radially symmetric. This problem could have been avoided if the two elements at the edge were replaced by a single triangular element, shown in Fig. 15.

Such representation would not have produced any information about the scalloping effect that occurs between the edge actuators. Another representation that would retain the radial symmetry and also provide a data point between the actuators would be the quadrilateral plate-bending element from SAP IV, shown in Fig. 16. In making the element compatible, it is subdivided into four smaller triangular elements with a common "sub-node" at the centroid of the element. Since the element is very skewed, almost to the point of becoming a triangle, some of the triangular sub-elements become very narrow leading to an overly stiff element. Thus, in the final representation, the quadrilateral element is replaced by two well-proportioned triangular elements. The use of two elements to represent this region of the mirror also allows for a reduction in the bandwidth of the global stiffness matrix.
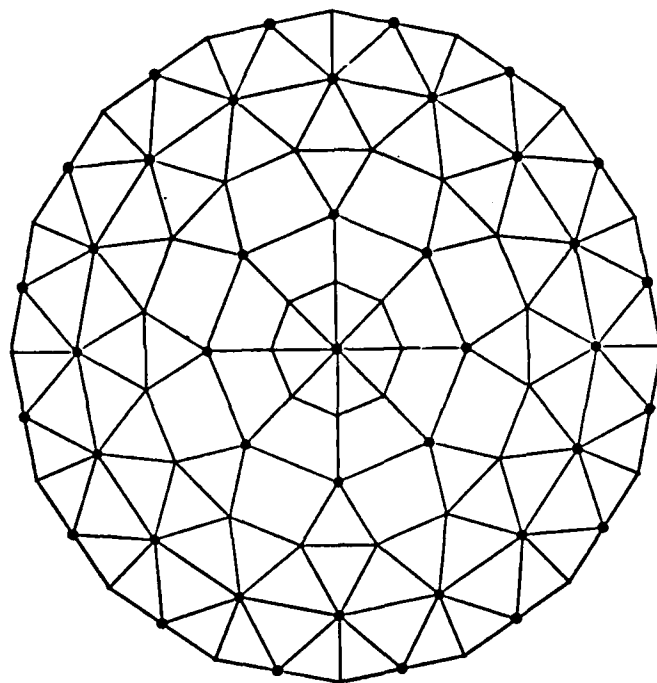
14

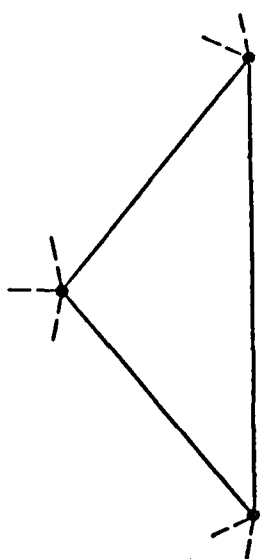Fig. 14. Finite element model of the mirror.
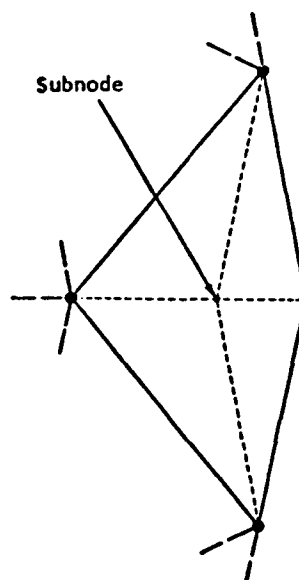

Fig. 15. Triangular edge element.

Fig. 16. The composition of the plate-bending quadrilateral element.

15

The membrane and bending stiffness of the actual shell are coupled. The convergence to shell action of the model, which is composed of triangular and flat quadrilateral plate elements (where the membrane and bending stiffness are uncoupled), has been demonstrated when the mesh size becomes increasingly small (Zienkiewicz, 1971, p. 238). The bending solution will converge non-monotonically while the membrane solution is monotonic in its convergence, yielding accurate results with a relatively coarse mesh.

Results

The deflection of the truss for in-plane slope control, shown (exaggerated) in Fig. 17, is a good illustration of the efficiency of tensile structures. Even though the actuator post is 6.8 mm in diameter and the wire only 0.81 mm in diameter, most of the angular deflection of the shell is produced not by the movement of the lower end of the post, as would be intuitively expected, but by the bending deflection of the post.

Figure 18(a, b, and c) illustrates the principle of the active mirror where the stiffnesses of the structure were chosen to make the deflections localized. These figures correspond to the normal position control of actuators A, B, and C of Fig. 10, respectively. Here the normalized deflections of the shell (dashed line) and the reference plate (dotted line) along the Y axis are superimposed. The mirror's deflection in all three cases is localized in a region of influence roughly one-fifth the mirror's diameter in size. The deflection of the reference plate in turn is more broad having less than 10% the magnitude of the shell's deflection for all load cases.
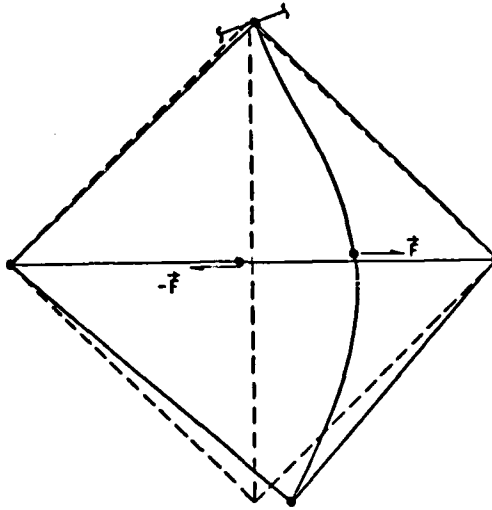
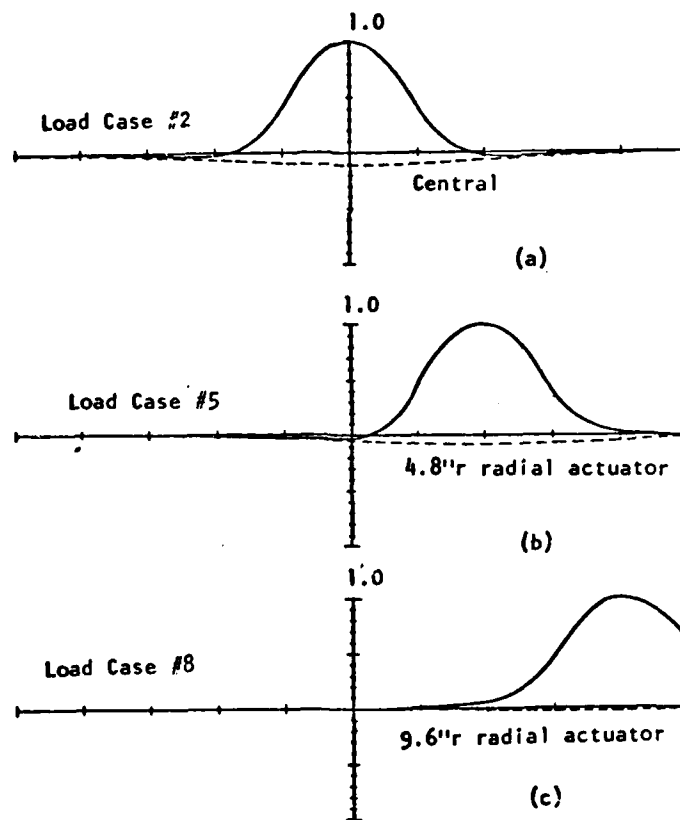Fig. 17. Truss deflections for in-plane slope control.

Fig. 18. Normalized mirror and reference plate deflections for normal position control.

Figures 19 through 29 are localized cubic spline fit contour plots from the normal and angular deflection data of the model of the shell. Normal position control, and tangential and radial slope control, for each unique actuator position were analyzed using unit loads. A small amount of scalloping can be seen in Fig. 20 where the contour curve near the edge is not circular. The amount of scalloping has been greatly reduced from that of the 9-actuator system (developed under a previous contract), thus illustrating the effectiveness of the edge actuators in reducing this effect.

Figures 30 through 40 are contour plots of the same load cases using the computer program FRINGE (Loomis, 1976). This program, ordinarily used to determine optical wavefront aberrations from interferometric data, makes a global Zernike polynomial fit using only the normal deflection data.

The Zernike polynomials are a complete set of polynomials in the two variables, r, θ, which are orthogonal over the interior of the unit circle. Their simple rotational symmetry properties lead to a polynomial product of the form

$$R(r) \ G(\theta),$$

where $G(\theta)$ is a continuous function that repeats itself every 2π radians and satisfies the requirement that rotating the coordinate system by an angle ϕ does not change the form of the polynomial, that is

$$G(\theta + \phi) \ = \ G(\theta)G(\phi).$$

The trigonometric function

$$G(\theta) \ = \ e^{+im\theta},$$

where m is any positive integer or zero, has the required properties. The radial function must be a polynomial in r of degree n and contain no power

18

Z Deflections

Contour Interval =
5.18 x 10^{-6}

Datum = 0.0

Fig. 19. Cubic spline contour plot of central actuator's slope control,
load case No. 1.

Z Deflections

Contour Interval = 0.160 x 10⁻⁶

Datum = 0.0

Fig. 20. Cubic spline contour plot of central actuator's normal position control, load case No. 2.

Z Deflections

Contour Interval =
0.167 x 10⁻⁴

Datum = 0.0

Fig. 21. Cubic spline contour plot of 4.8"r actuator's tangential slope control, load case No. 3.

Z Deflections

Contour Interval = 0.566 x 10^{-5}

Datum = 0.0

Fig. 22. Cubic spline contour plot of 4.8"r actuator's radial clope control, load case No. 4.

Z Deflections

Contour Interval =
0.566 x 10⁻⁵

Datum = 0.0

Fig. 23. Cubic spline contour plot of 4.8"r actuator's normal position
control, load case No. 5.

Z Deflections

Contour Interval = 0.133 x 10⁻⁴

Datum = 0.0

Fig. 24.   Cubic spline contour plot of 9.6"r actuator's tangential slope
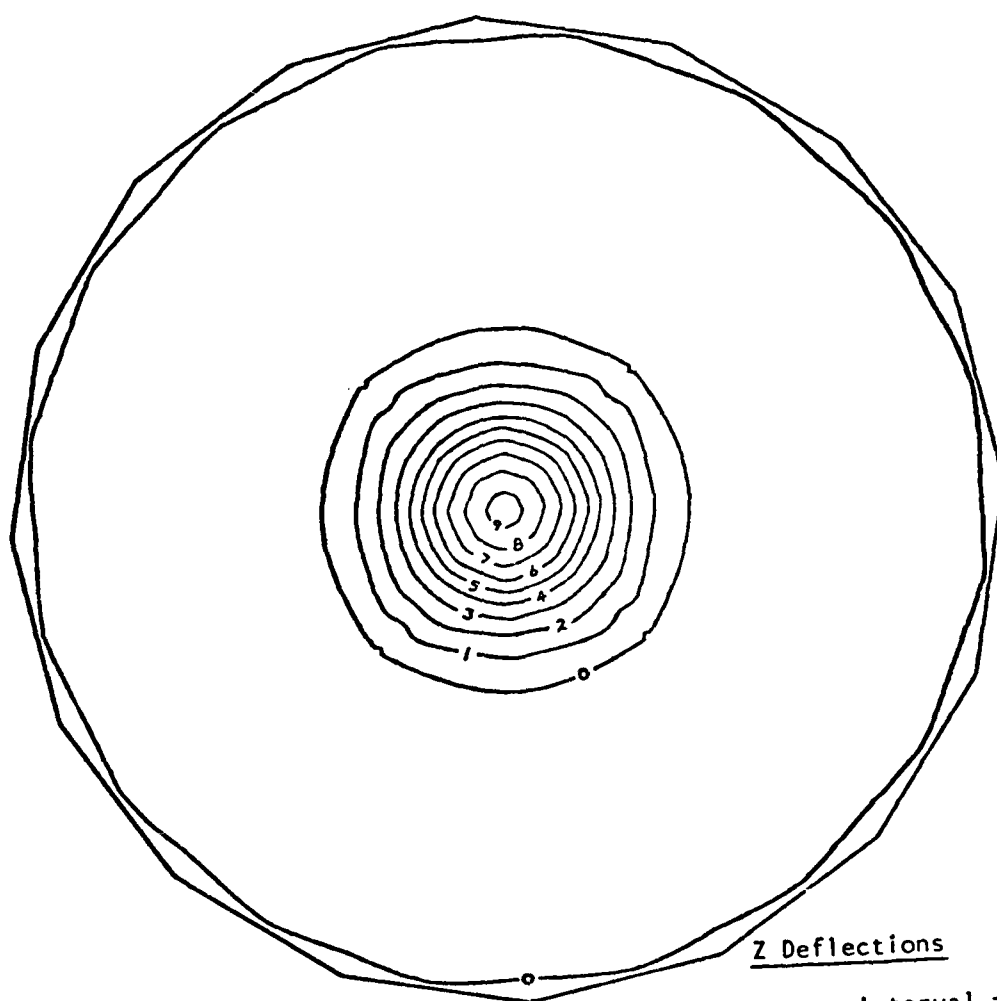control, load case No. 6.
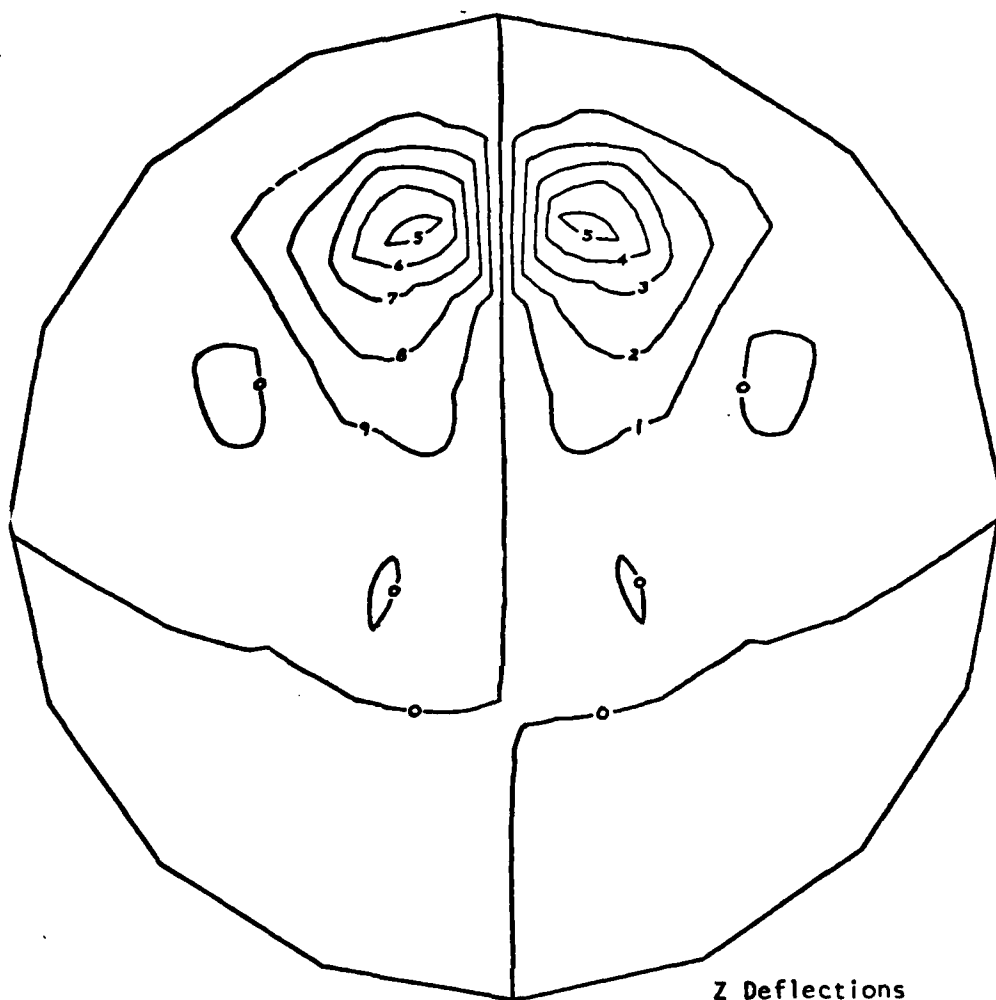
24

Z Deflections

Contour Interval =
0.958 x 10^{-5}

Datum = 0.0

Fig. 25.   Cubic spline contour plot of 9.6"r actuator's radial slope control,
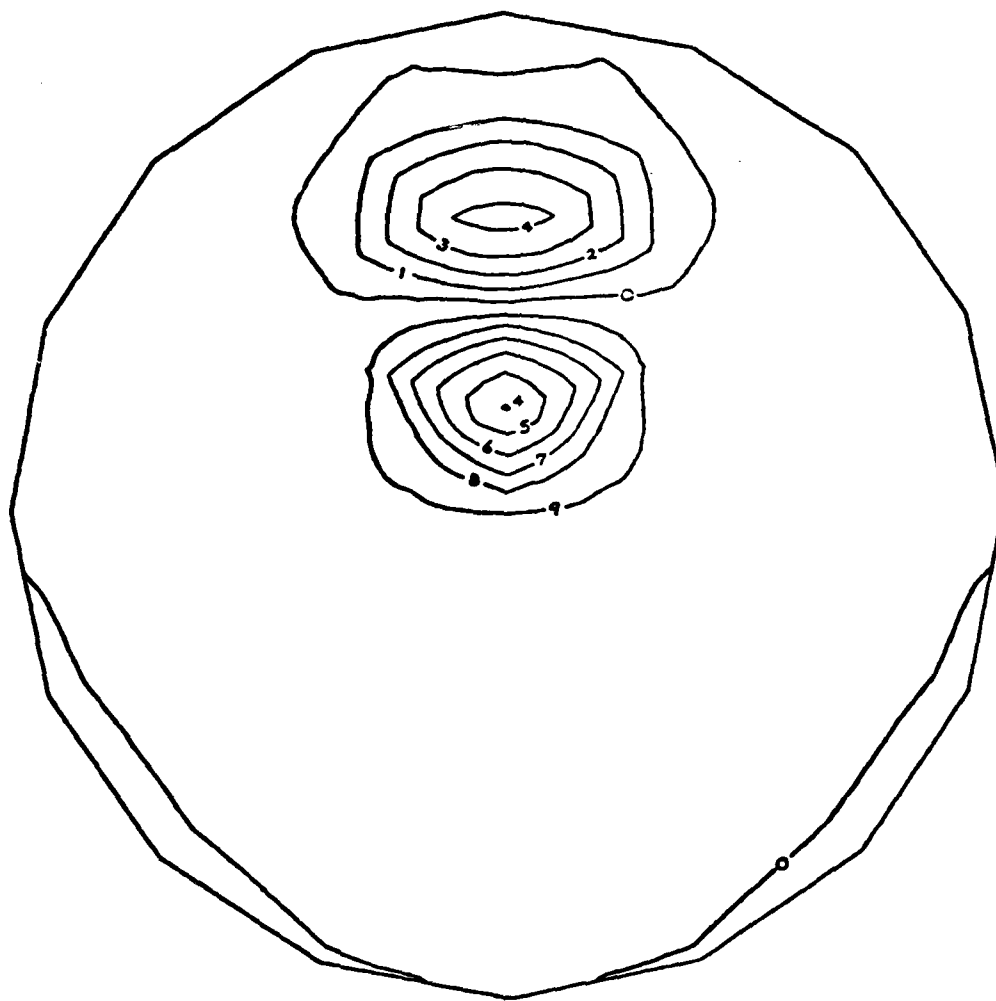load case No. 7.

Z Deflections

Contour Interval =
0.228 x 10^{-6}

Datum = 0.0

Fig. 26.   Cubic spline contour plot of 9.6"r actuator's normal position
control, load case No. 8.

Z Deflections

Contour Interval =
0.333 × 10⁻⁵

Datum = 0.0

Fig. 27.   Cubic spline contour plot of edge actuator's tangential slope
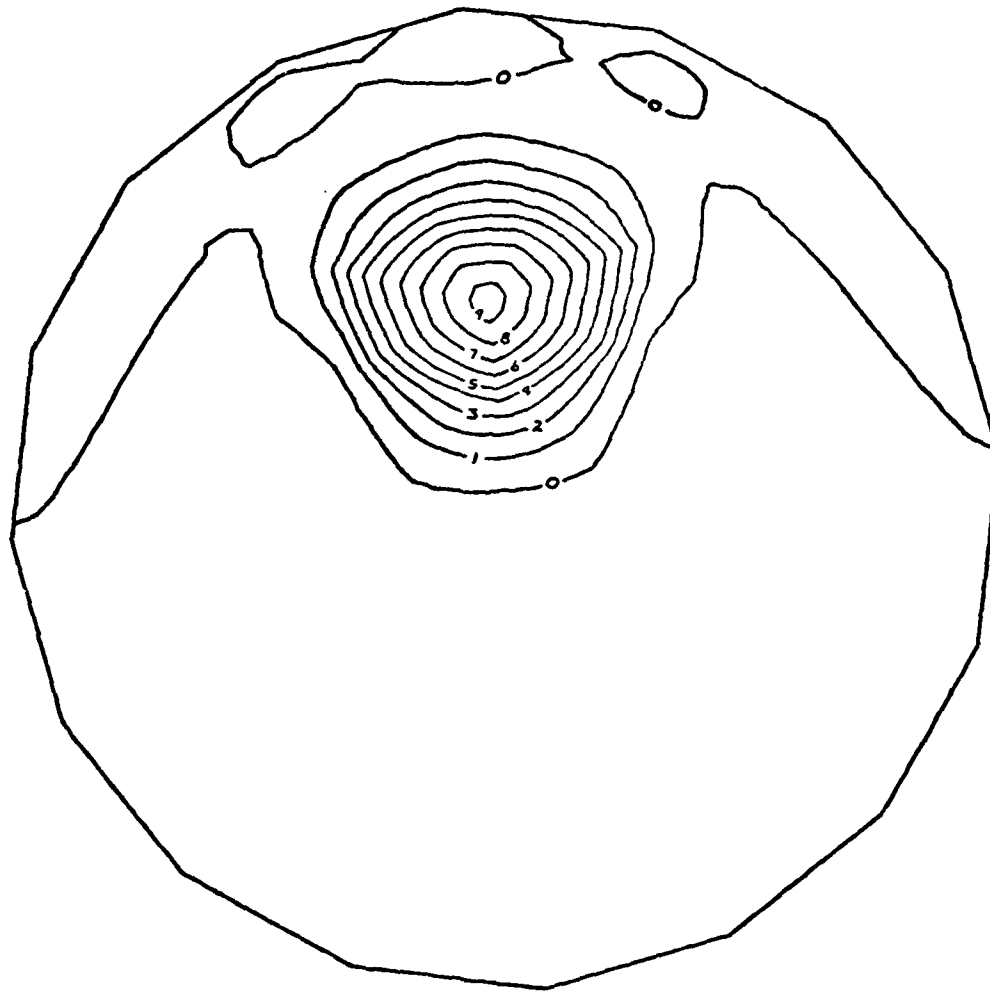control, load case No. 9.

Z Deflections

Contour Interval =
0.173 x 10^{-4}

Datum = 0.0

Fig. 28. Cubic spline contour plot of edge actuator's radial slope control,
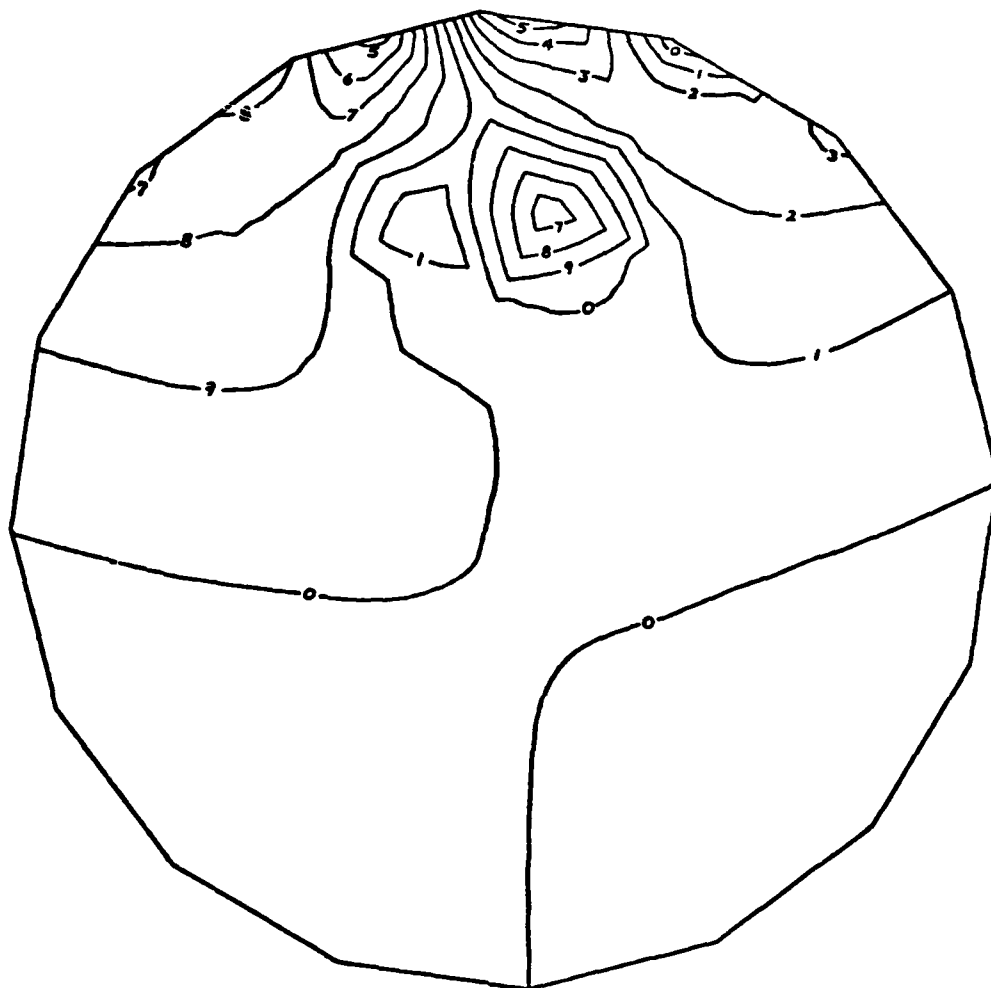load case No. 10.

Z Deflections

Contour Interval =
0.285 x 10^{-6}

Datum = 0.0

Fig. 29. Cubic spline contour plot of edge actuator's normal position
control, load case No. 11.

Z Deflections

Contour Interval = 5.18×10^{-6}

Datum = 0

Fig. 30.   Zernike polynomial contour plot of central slope control, load case No. 1. (Note: Figs. 30 through 40 contain plotter errors in FRINGE.)

Z Deflections

Contour Interval =
0.160 x 10^{-6}

Datum = 0

Fig. 31. Zernike polynomial contour plot of central position control,
load case No. 2.

Z Deflections

Contour Interval =
0.167 x 10^{-4}

Datum = 0

Fig. 32. Zernike polynomial plot of tangential slope control of 4.8"r actuator, load case No. 3.
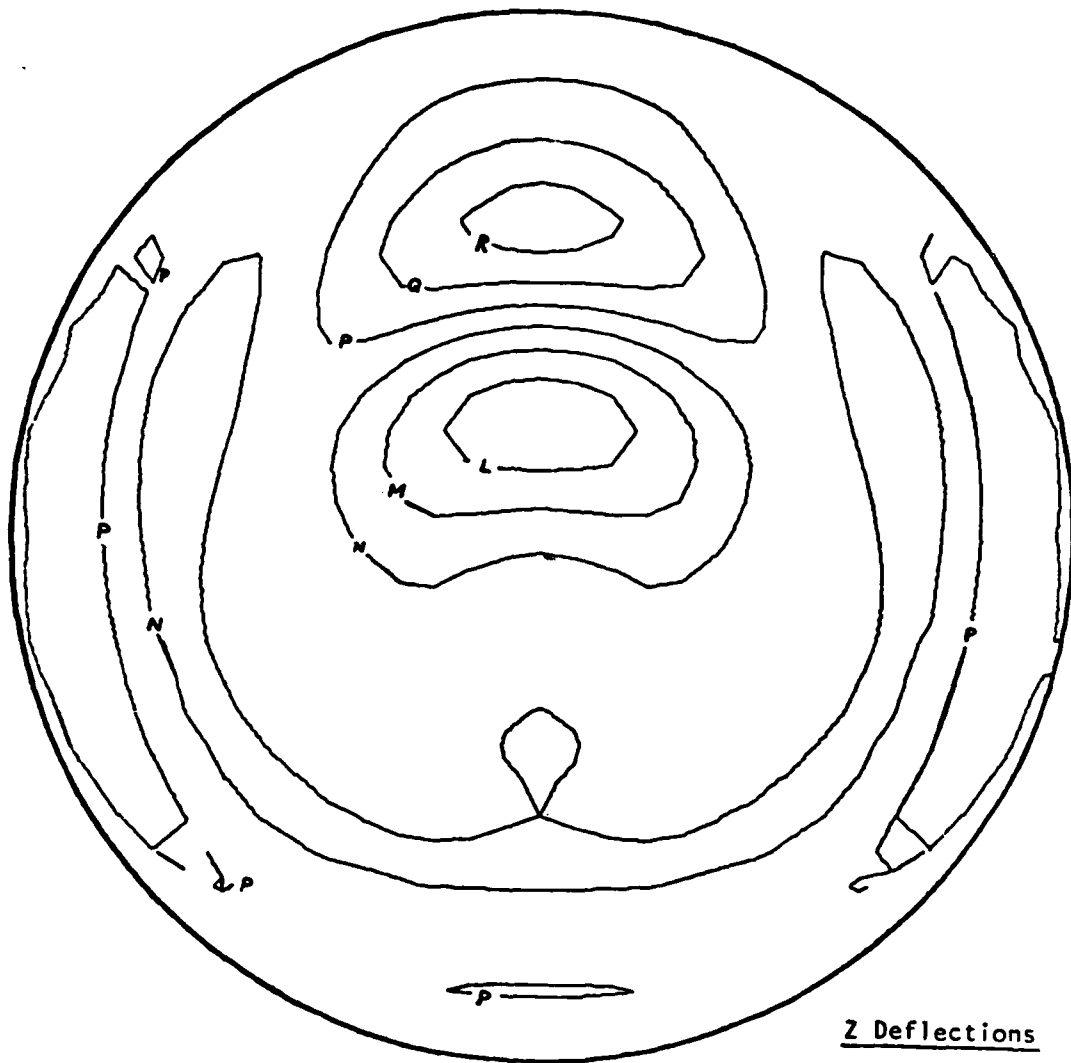
Z Deflections

Contour Interval =
0.566×10^{-5}

Datum = 0

Fig. 33. Zernike polynomial plot of 4.8"r actuator radial slope control, load case No. 4.
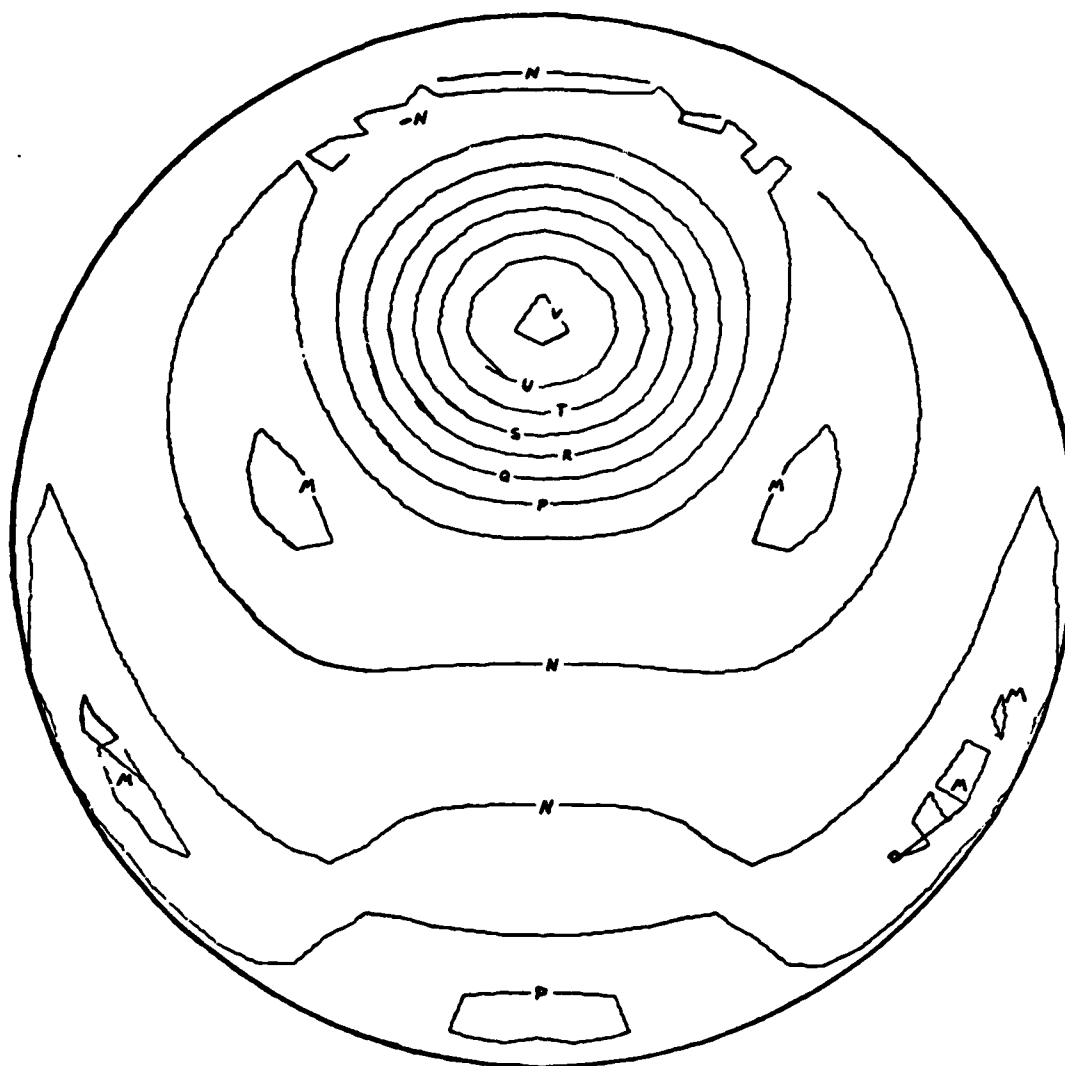
Z Deflections

Contour Interval =
0.566×10^{-5}

Datum = 0

Fig. 34. Zernike polynomial contour plot of 4.8"r actuator's normal position control, load case No. 5.

Z Deflections

Contour Interval =
0.133 x 10^{-4}

Datum = 0

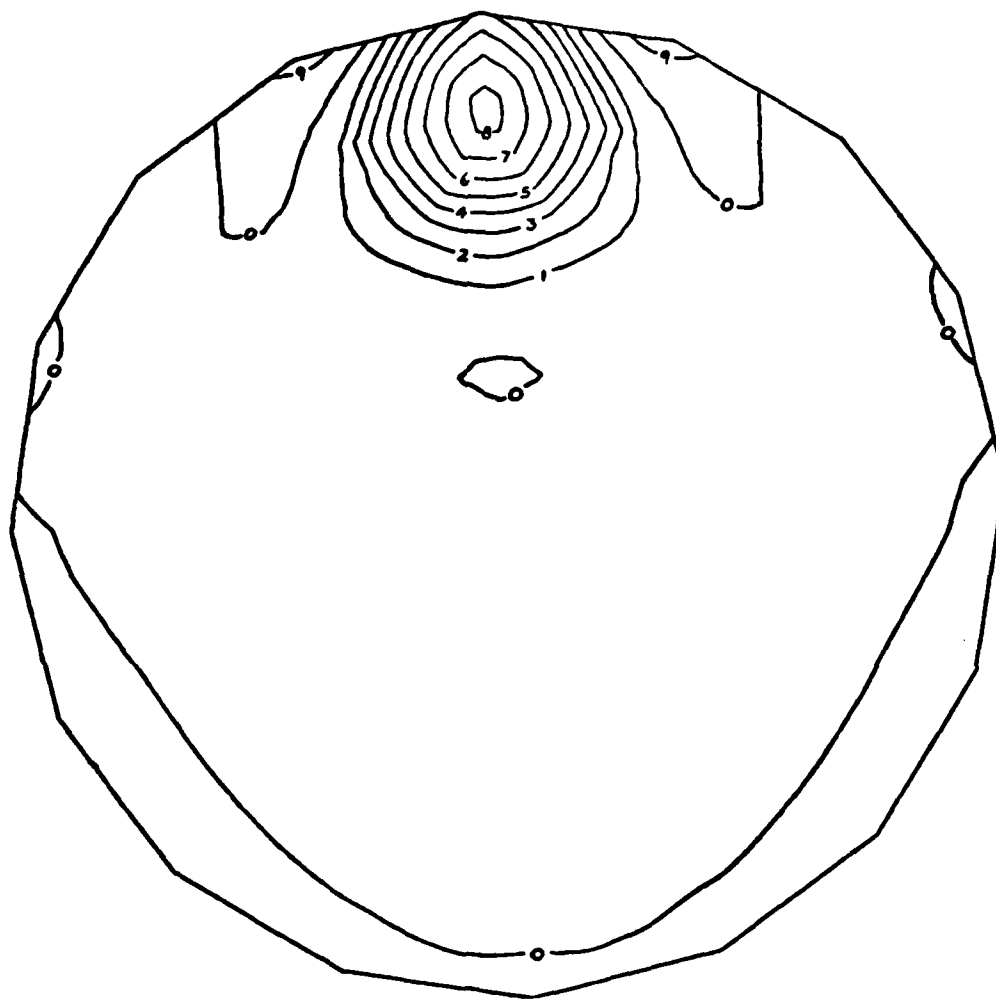Fig. 35. Zernike polynomial plot of 9.6"r actuator's tangential slope control, load case No. 6.
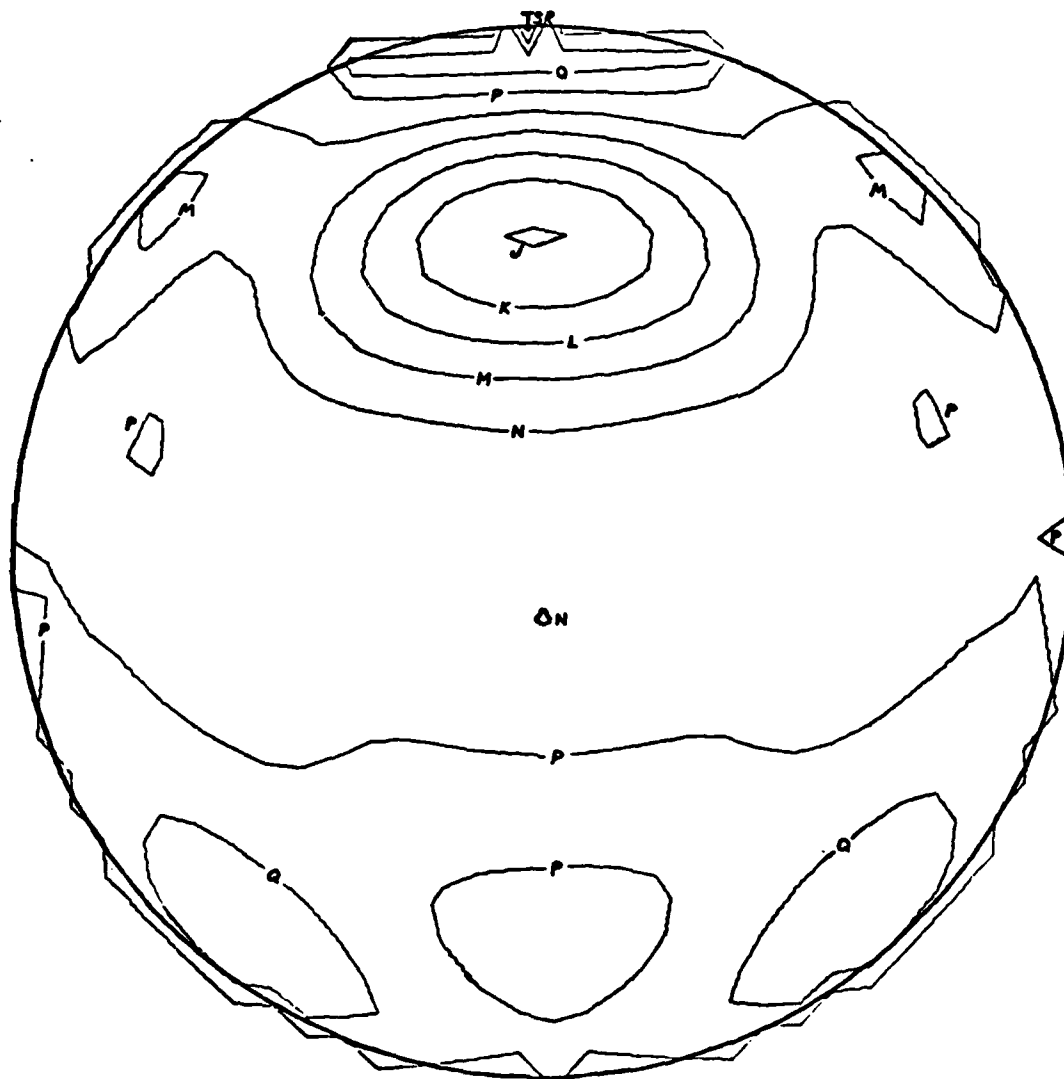
Z Deflections

Contour Interval =
0.958×10^{-5}

Datum = 0

Fig. 36. Zernike polynomial contour plot of 9.6"r actuator's radial slope
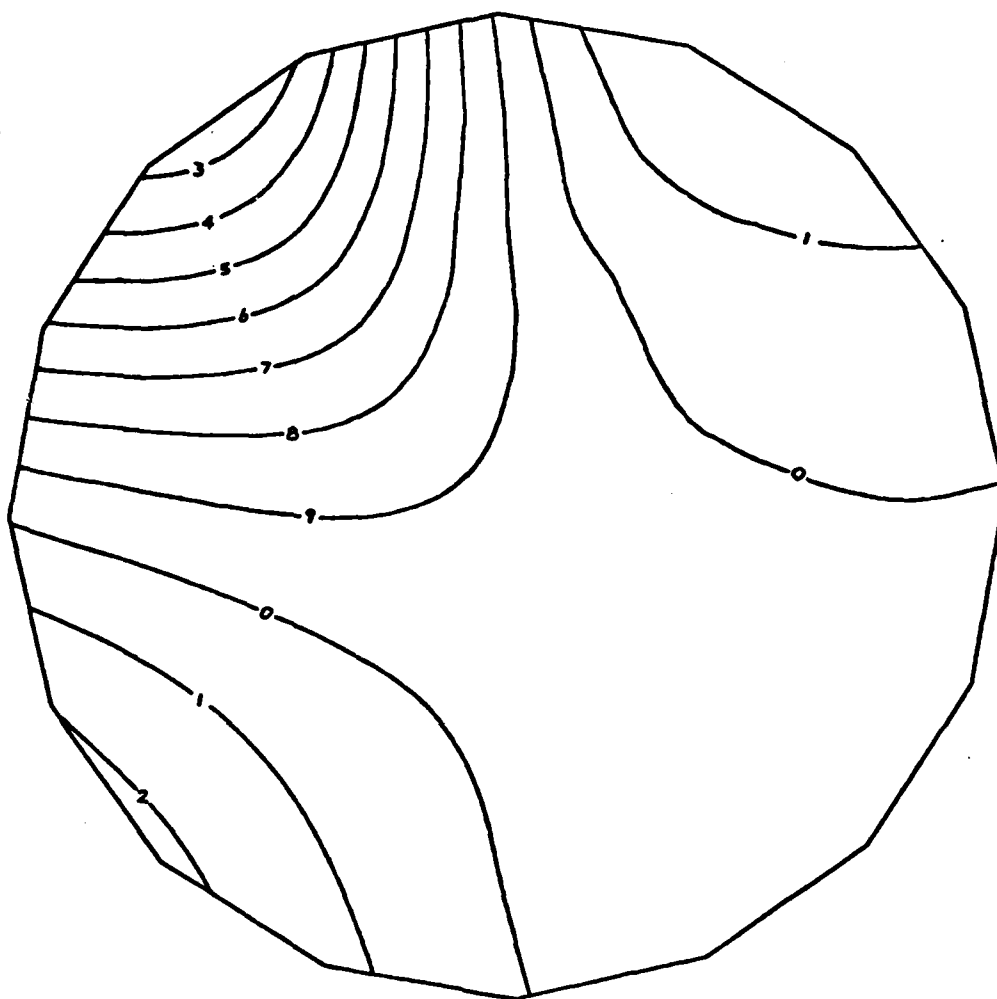control, load case No. 7.
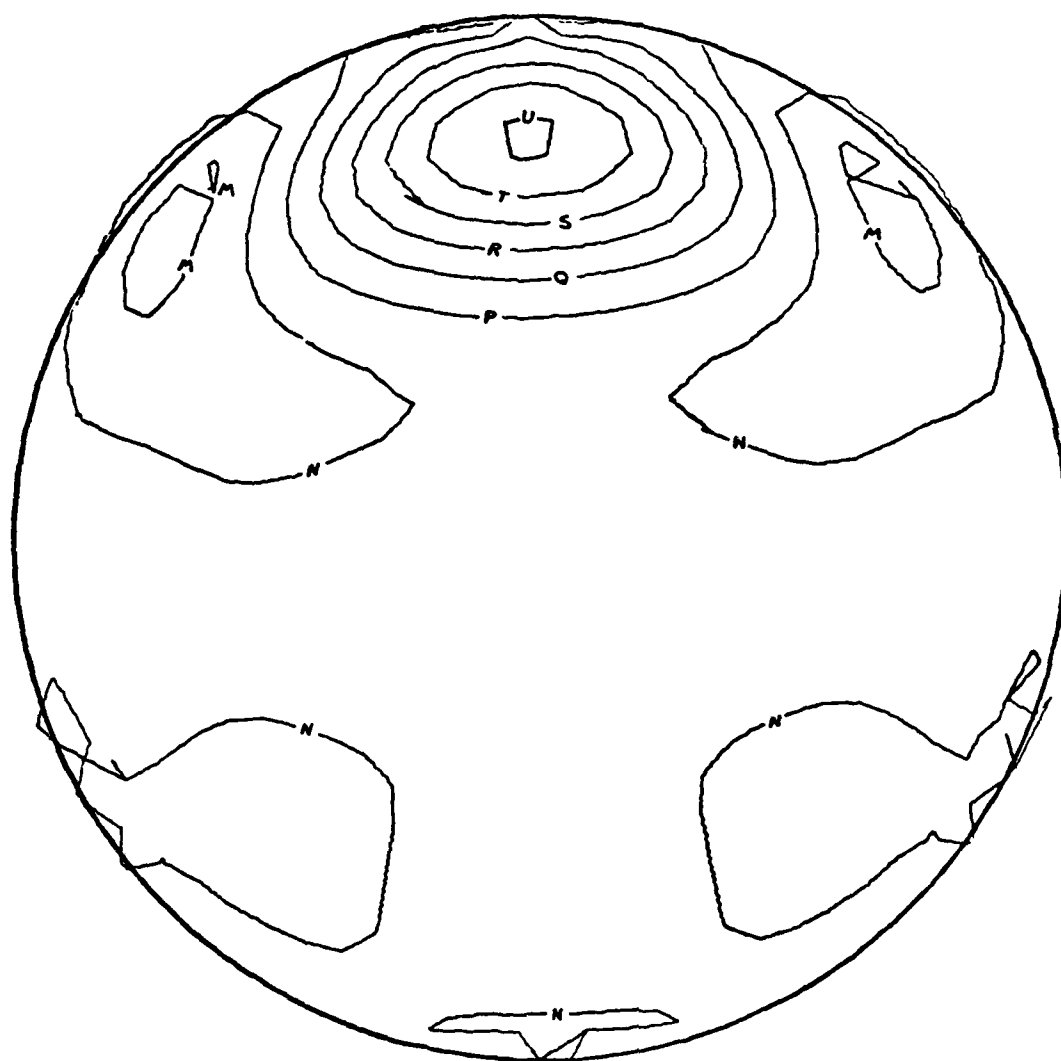
Z Deflections

Contour Interval =
0.228 x 10^{-6}

Datum = 0

Fig. 37. Zernike polynomial contour plot of 9.6"r actuator's normal position
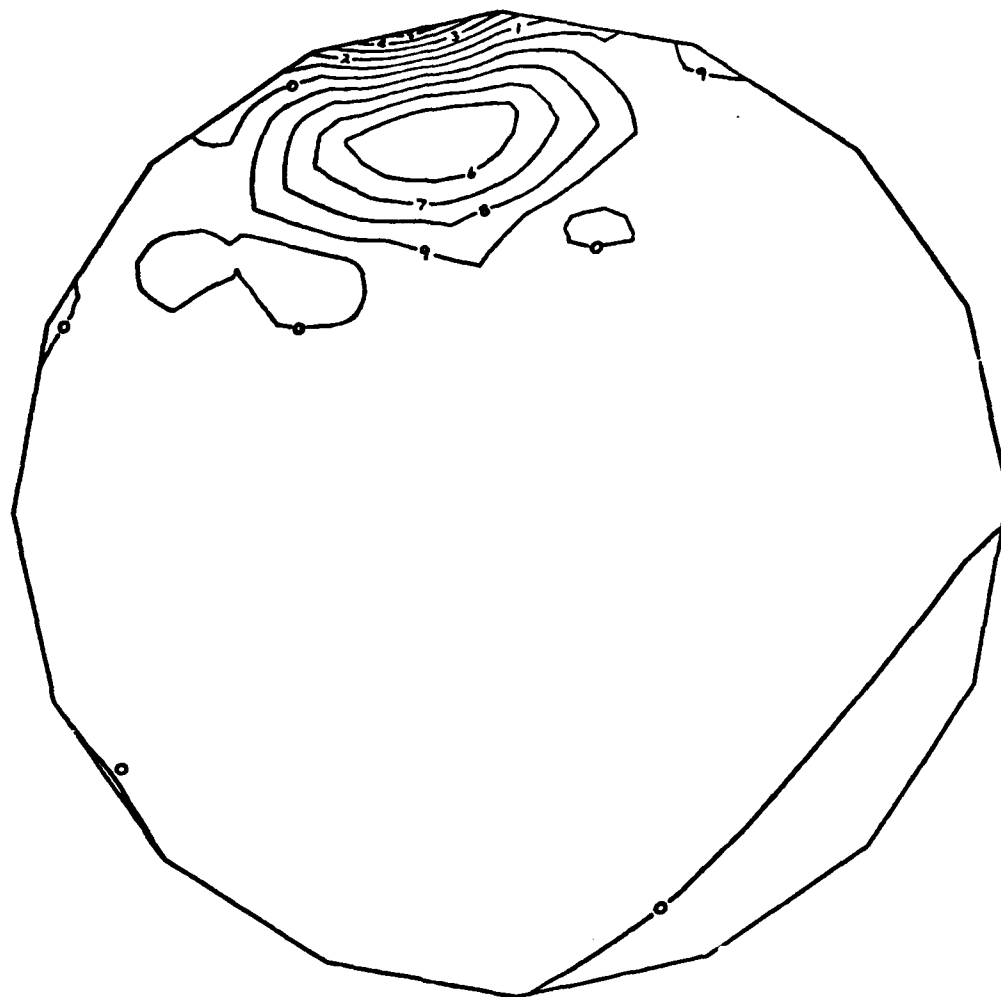control, load case No. 8.
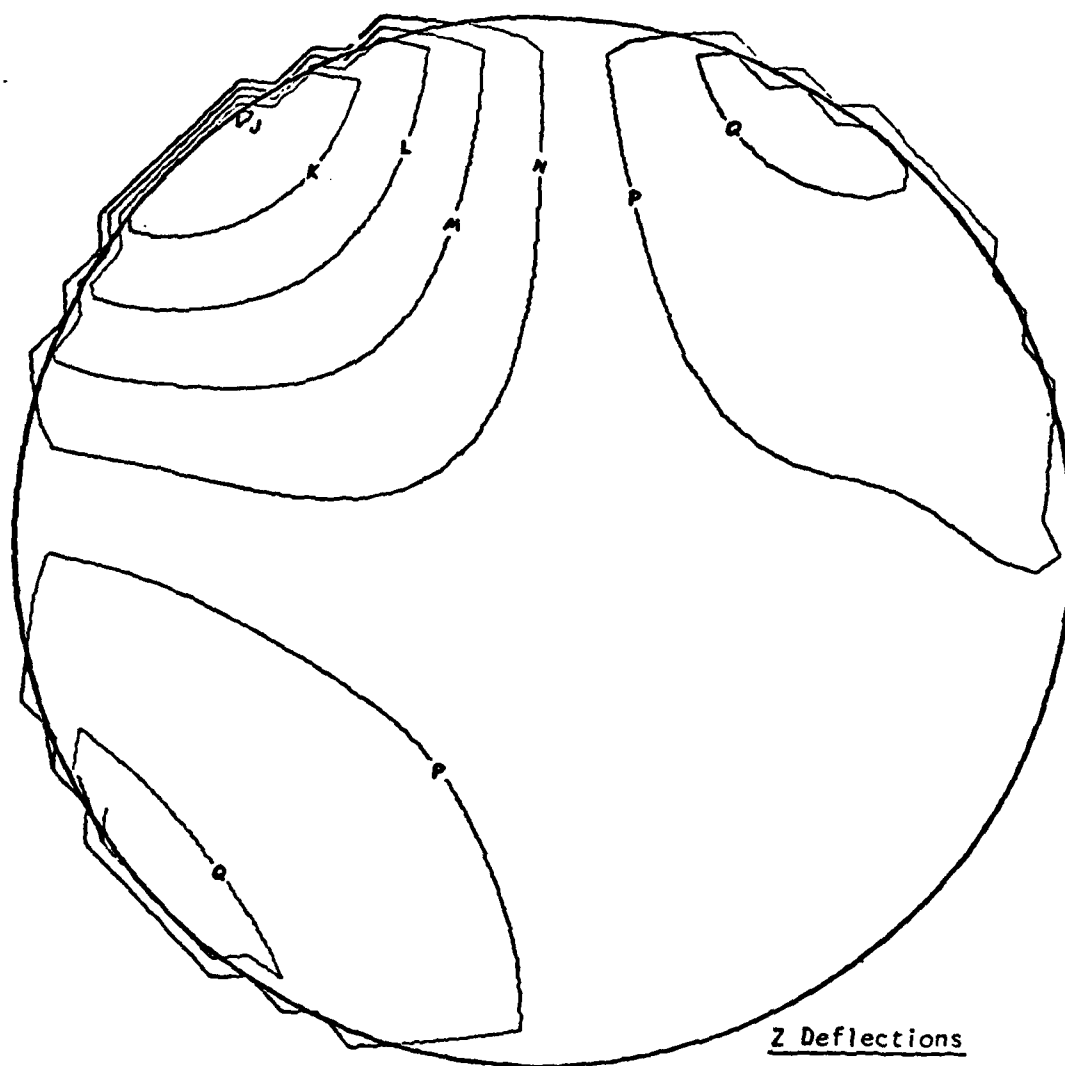
Z Deflections

Contour Interval =
0.333×10^{-5}

Datum = 0

Fig. 38. Zernike polynomial contour plot of edge actuator's tangential slope
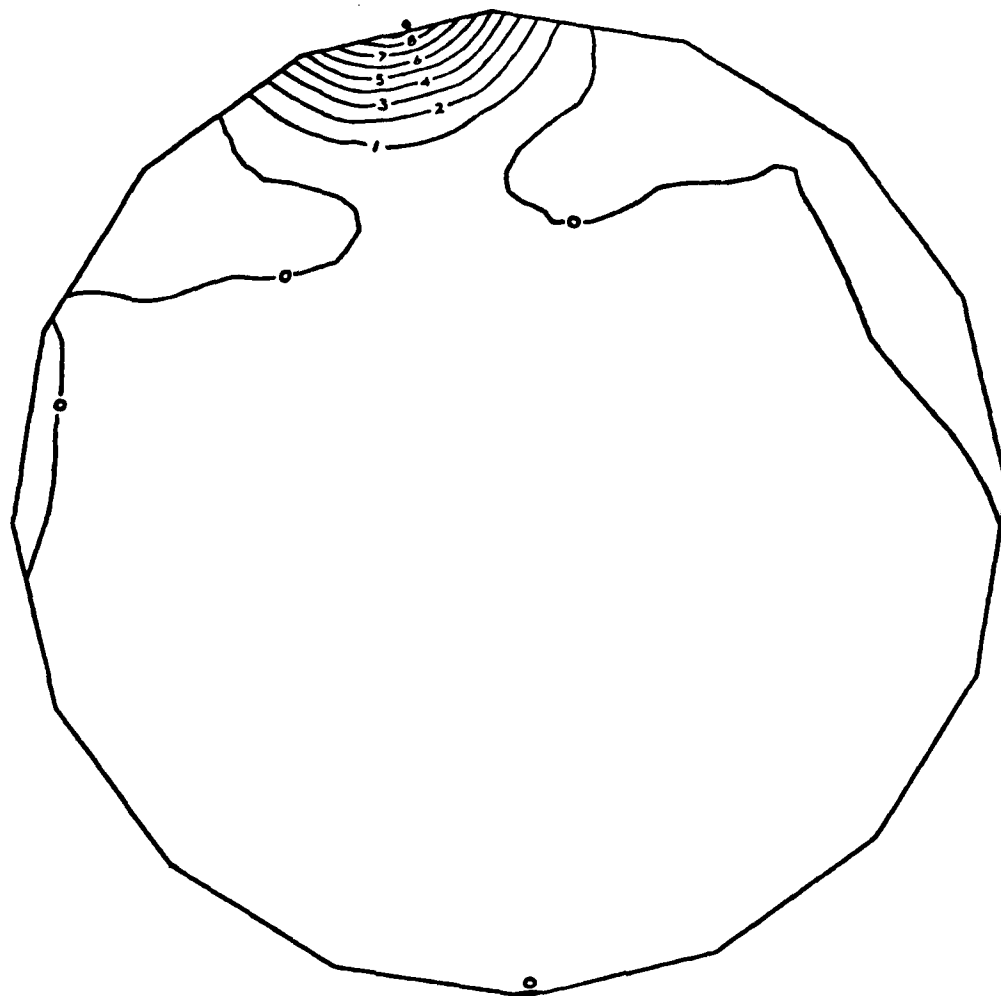control, load case No. 9.
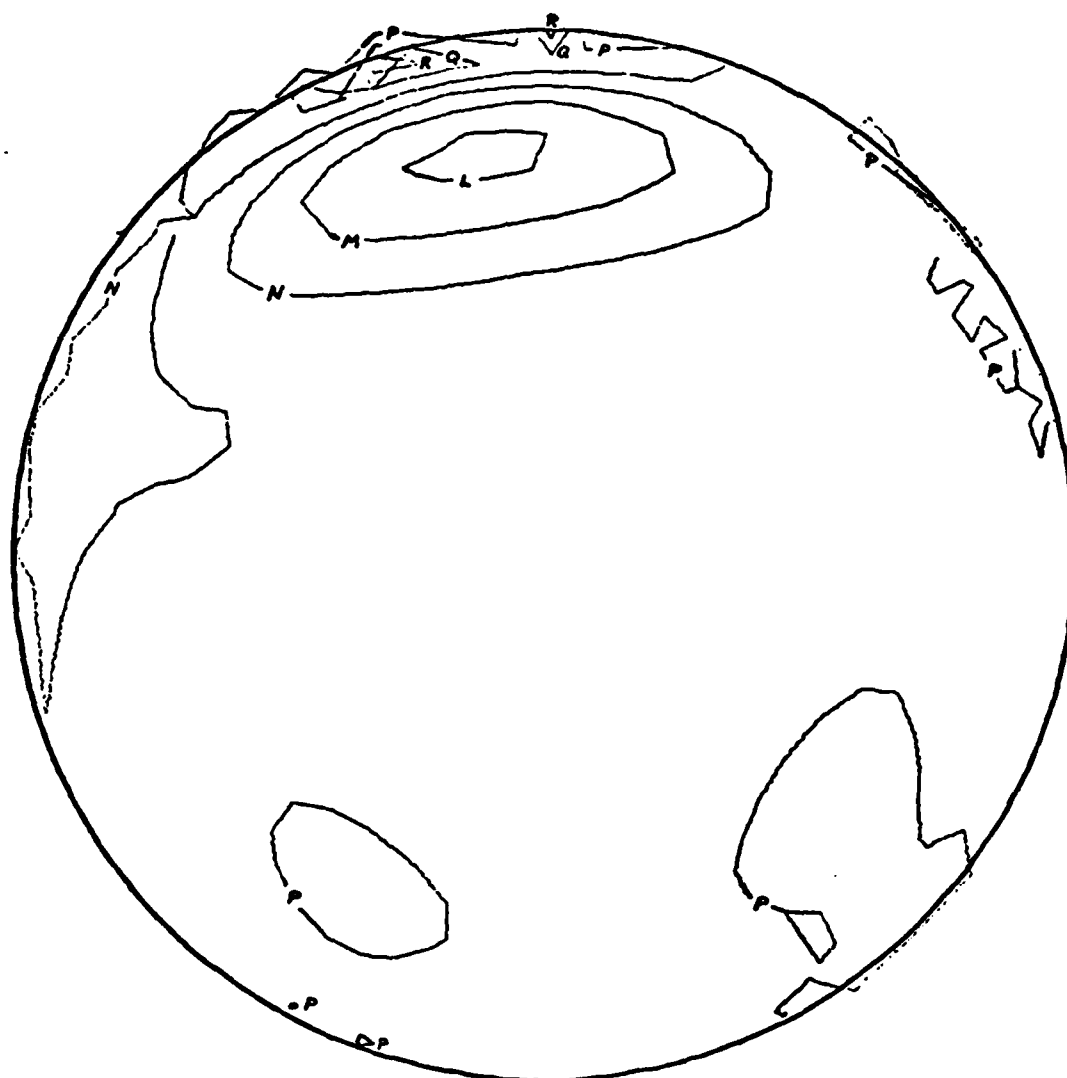
Z Deflections

Contour Interval =
0.173 x 10^{-4}

Datum = 0

Fig. 39. Zernike polynomial contour plot of edge actuator's radial slope
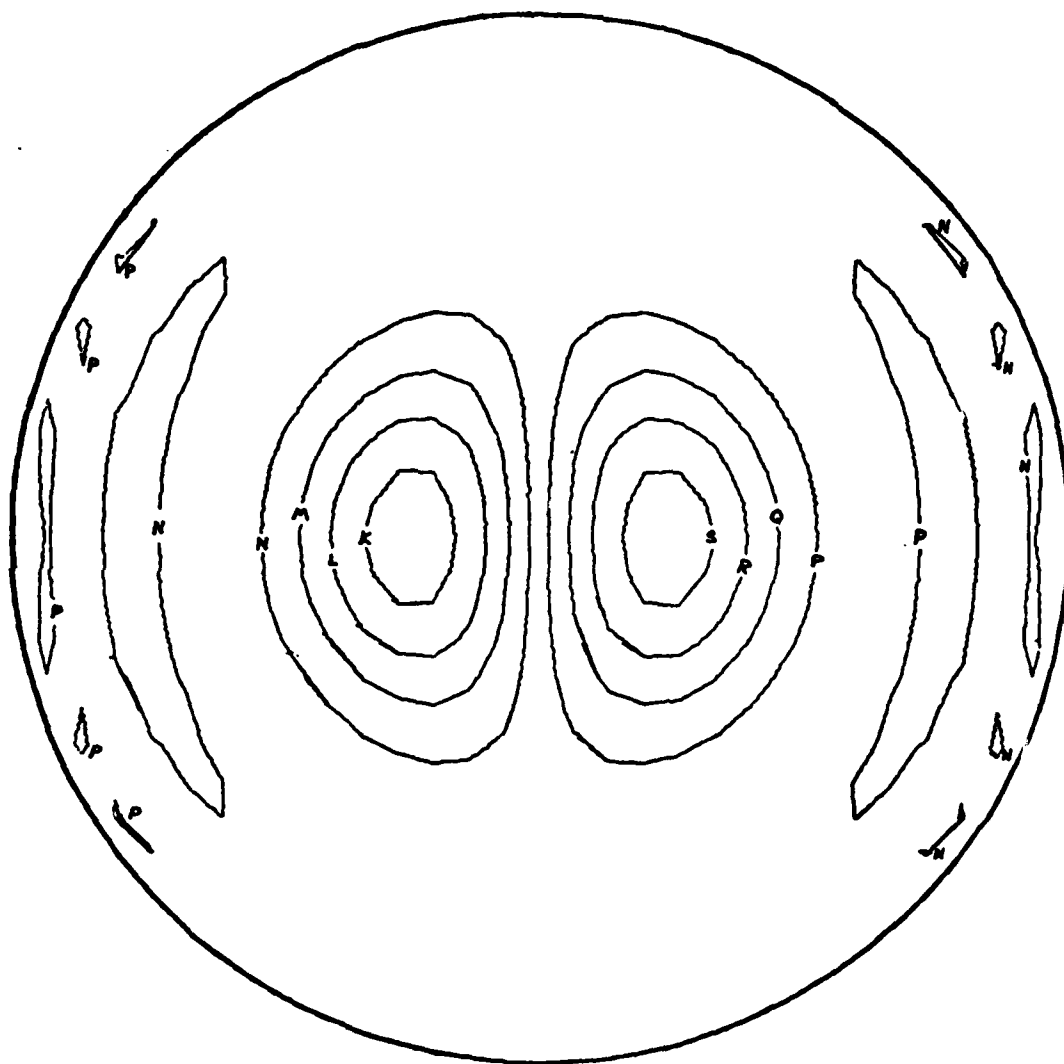control, load case No. 10.

Z Deflections
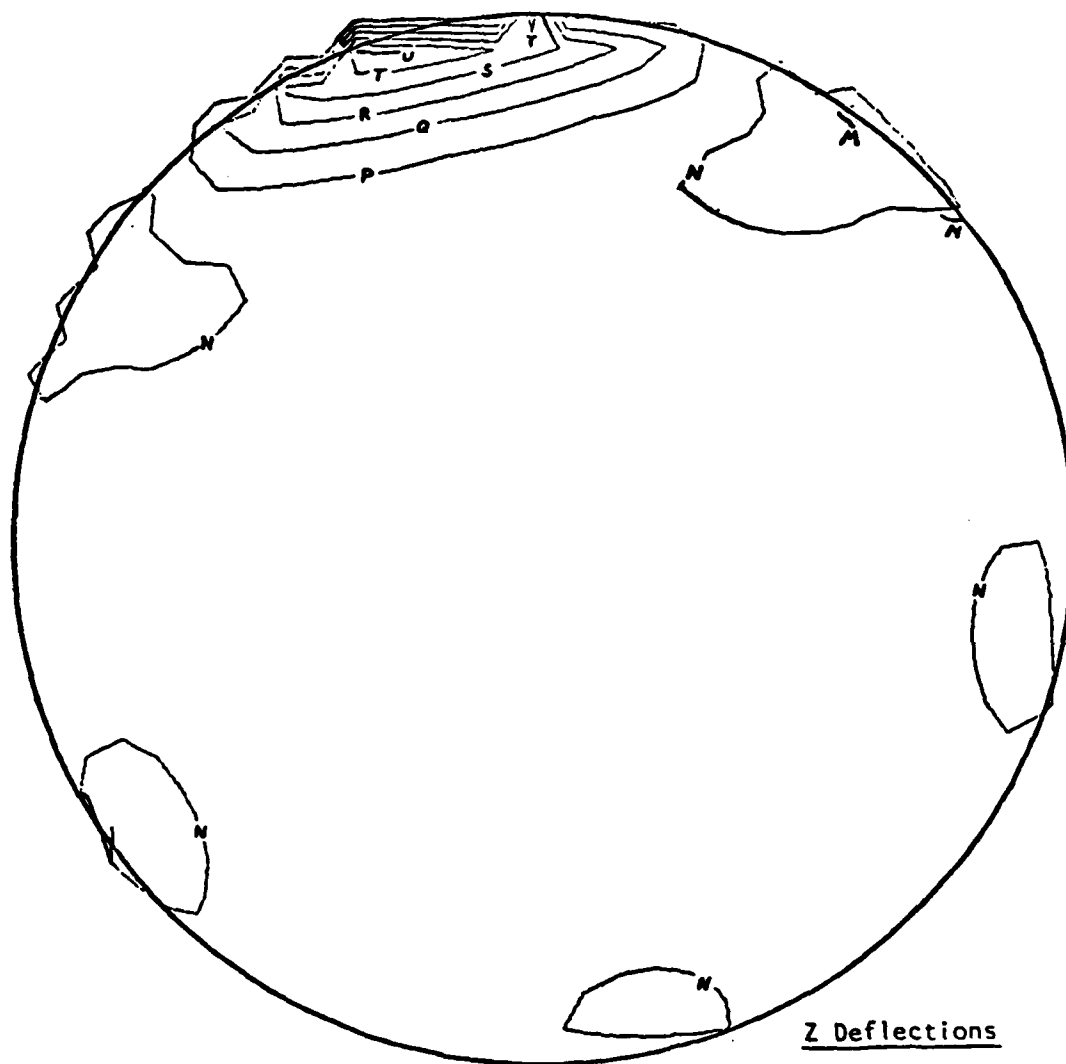
Contour Interval =
0.285 x 10⁻⁶

Datum = 0

Fig. 40. Zernike polynomial contour plot of edge actuator's normal position
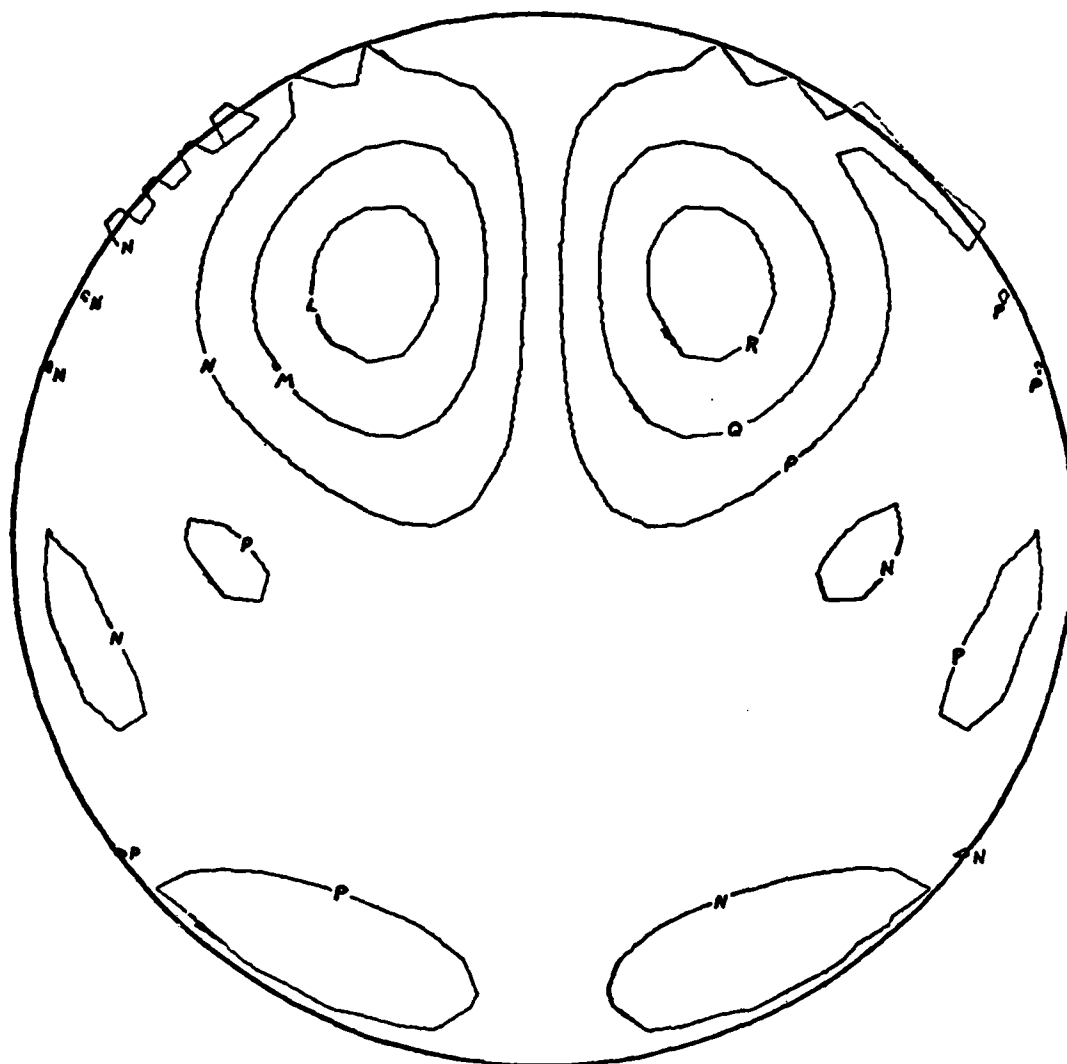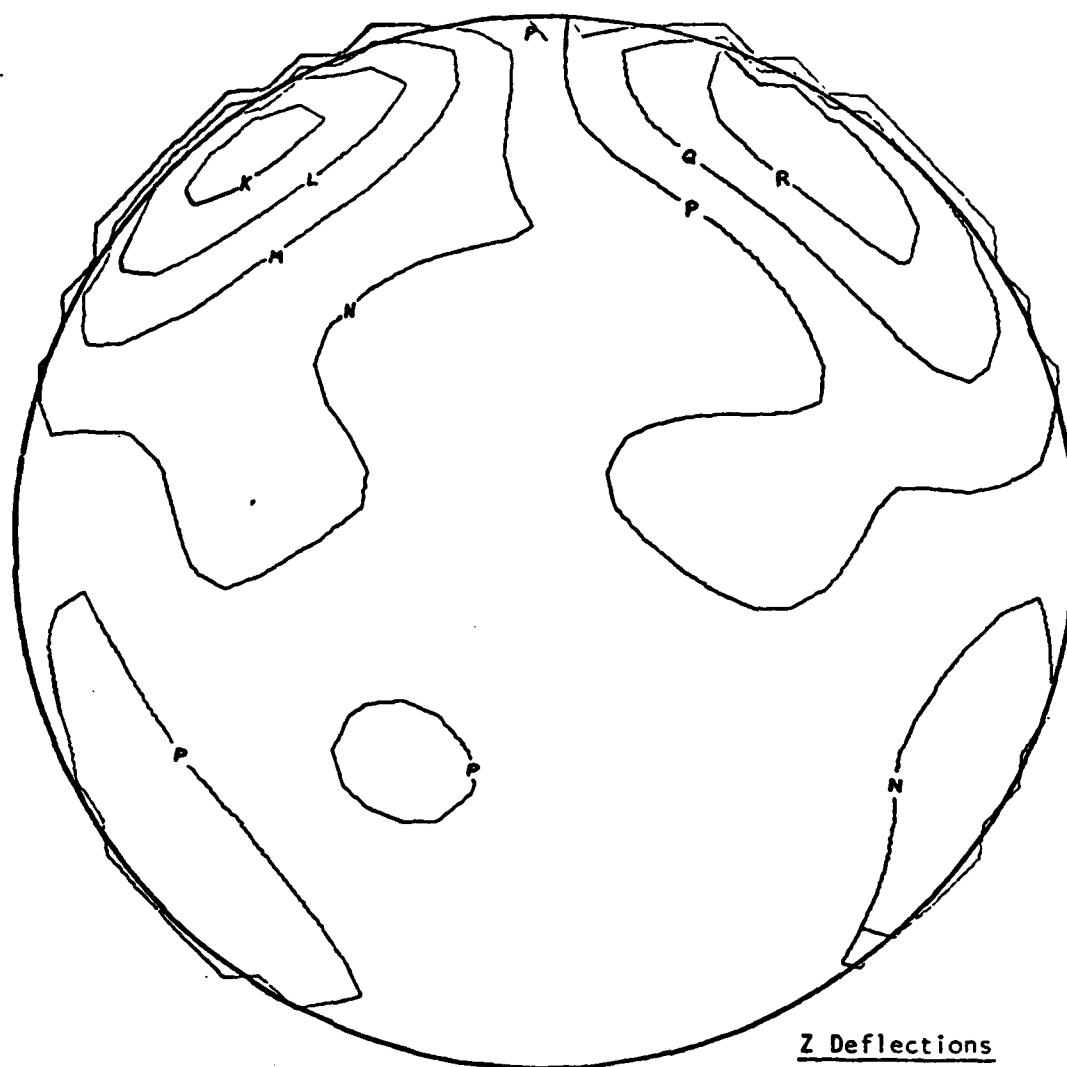control, load case No. 11.

of r less than m. R(r) must also be even if m is even and odd if m is odd.

The radial polynomials can be derived as a special case of Jacobi or hypergeometric polynomials and tabulated as $R_n^m(r)$. Their orthogonality and normalization properties are given by

$$\int_o^1 R_n^m(r) \ R_{n1}^m(r) r \ dr = \frac{1}{2(n+1)} \ \delta_{nn1} \ ,$$

where δ_{nn1} is the Kronecker delta, and $R_n^m(1) = 1$.

To simplify the computation of the Zernike polynomials, we factor the radial polynomial into

$$R_{2n-m}^{\ m} \ (r) = Q_n^m(r) \ r^m \ ,$$

where $Q_n^m(r)$ is a polynomial of order $2(n-m)$. This polynomial can be generally written as

$$Q_n^m(r) = \sum_{s=o}^{n-m} (-1)^s \ \frac{(2n-m-s)!}{s!(n-s)!(n-m-s)!} \ r^{2(n-m-s)} .$$

The final Zernike polynomial series may be written

$$\Delta Z = \overline{\Delta Z} + \sum_{n=1}^{\infty} \left[A_n Q_n^O \ (r) \ + \ \sum_{m=1}^{n} Q_n^m(r) \ r^m (B_{nm} \ \cos m\theta \ + \ C_{nm} \ \sin m\theta) \right]$$

where $\overline{\Delta Z}$ is the mean deflection of the mirror surface (or the mean wavefront optical path difference) and A_n, B_{nm}, and C_{nm} are individual polynomial co-efficients.

Table 1 lists the modified circular polynomials in a Pascal's triangle manner and Table 2 lists the Zernike polynomials used by FRINGE. It is seen in Table 2 that the highest order angular terms (terms 25 and 26) have for an

41

Table 1. Modified Circle Polynomials $Q_n^m(r)$

n \ m	0	1	2	3	4	5
0	1					
1	$2r^2 - 1$	1				
2	$6r^4 - 6r^2 + 1$	$3r^2 - 2$	1			
3	$20r^6 - 30r^4 + 12r^2 - 1$	$10r^4 - 12r^2 + 3$	$4r^2 - 3$	1		
4	$70r^8 - 140r^6 + 90r^4 - 20r^2 + 1$	$35r^6 - 60r^4 + 30r^2 - 4$	$15r^4 - 20r^2 + 6$	$5r^2 - 4$	1	
5	$252r^{10} - 630r^8 + 560r^6 - 210r^4 + 30r^2 - 1$	$126r^8 - 280r^6 + 210r^4 - 60r^2 + 5$	$56r^6 - 105r^4 + 60r^2 - 10$	$21r^4 - 30r^2 + 10$	$6r^2 - 5$	1

Table 2. Zernike Polynomials Used by FRINGE

No	Polynomial
0	1
1	$r \cos\theta$
2	$r \sin\theta$
3	$2 r^2 - 1$
4	$r^2 \cos 2\theta$
5	$r^2 \sin 2\theta$
6	$(3r^2 - 2) \, r \cos\theta$
7	$(3r^2 - 2) \, r \sin\theta$
8	$6 r^4 - 6 r^2 + 1$
9	$r^3 \cos 3\theta$
10	$r^3 \sin 3\theta$
11	$(4 r^2 - 3) \, r^2 \cos 2\theta$
12	$(4 r^2 - 3) \, r^2 \sin 2\theta$
13	$(10 r^4 - 12 r^2 + 3) \, r \cos\theta$
14	$(10 r^4 - 12 r^2 + 3) \, r \sin\theta$
15	$20 r^6 - 30 r^4 + 12 r^2 - 1$
16	$r^4 \cos 4\theta$
17	$r^4 \sin 4\theta$
18	$(5 r^2 - 4) \, r^3 \cos 3\theta$
19	$(5 r^2 - 4) \, r^3 \sin 3\theta$
20	$(15 r^4 - 20 r^2 + 6) \, r^2 \cos 2\theta$
21	$(15 r^4 - 20 r^2 + 6) \, r^2 \sin 2\theta$
22	$(35 r^6 - 60 r^4 + 30 r^2 - 4) \, r \cos\theta$
23	$(35 r^6 - 60 r^4 + 30 r^2 - 4) \, r \sin\theta$
24	$70 r^8 - 140 r^6 + 90 r^4 - 20 r^2 + 1$
25	$r^5 \cos 5\theta$
26	$r^5 \sin 5\theta$
27	$(6 r^2 - 5) \, r^4 \cos 4\theta$
28	$(6 r^2 - 5) \, r^4 \sin 4\theta$
29	$(21 r^4 - 30 r^2 + 10) \, r^3 \cos 3\theta$
30	$(21 r^4 - 30 r^2 + 10) \, r^3 \sin 3\theta$
31	$(56 r^6 - 105 r^4 + 60 r^2 - 10) \, r^2 \cos 2\theta$
32	$(56 r^6 - 105 r^4 + 60 r^2 - 10) \, r^2 \sin 2\theta$
33	$(126 r^8 - 280 r^6 + 210 r^4 - 60 r^2 + 5) \, r \cos\theta$
34	$(126 r^8 - 280 r^6 + 210 r^4 - 60 r^2 + 5) \, r \sin\theta$
35	$252 r^{10} - 630 r^8 + 560 r^6 - 210 r^4 + 30 r^2 - 1$
36	$924 r^{12} - 2772 r^{10} + 3150 r^8 - 1680 r^6 + 420 r^4 - 42 r^2 + 1$

argument 5θ. Since there are 16 edge actuators, the angular terms would need
to have arguments up to and including 8θ to properly represent just the radially
symmetric scalloping effect near the edge of the mirror.

Table 3 lists the Zernike polynomial coefficients for all 11 load cases.
A description of each load case is given in the captions of the contour plots.
The radially symmetric load case No. 2 has five dominant coefficients of pure
radial polynomials and two relatively small coefficients of polynomials with
angular dependence. Since both angular polynomials have arguments of 4θ, a
small amount of scalloping exists in the region of the eight actuators that
correspond to actuator "B" in Fig. 10. A better representation of the scal-
loping for this load case would not require the use of a complete set of
higher order polynomials since the symmetry and angular dependence properties
of the deflections are already known.

Table 4 illustrates the convergence of the polynomial approximations by
listing the root-mean-square (i.e., RMS) of the error between the polynomial
and the data points for various orders of complete sets of the polynomials
used. The deflections of load case No. 2 are represented very accurately by
a 36-term set while that of the radially asymmetric deflections of load case
No. 1. has its RMS error reduced only by a factor of three for the same number
of terms. The cubic spline contours for these load cases (Figs. 19 and 20) show
that both are localized within regions of comparable size, while those of the
global polynomial approximation show the deflection of load case No. 1 (Fig.
31) to be more broad than that of load case No. 2 (Fig. 32). The inability
of the 36-term polynomial approximation to represent this asymmetric deflection
in a localized manner is due to the relatively low order of the radial

44

Table 3. Zernike Polynomial Coefficients in Wavelengths

Term No.	1	2	3	4	5	6	7	8	9	10	11
1	+.11467	0.0	+.36439	+.00028	-.00002	+.40415	.00000	+.00002	+.16387	-.02838	-.00140
2	+.00031	0.0	+.00336	+.07287	+.00524	-.07237	-.33884	+.00889	-.20264	-.30507	+.00608
3	0.0	-.00130	+.00067	+.17352	-.00405	-.00617	+.15346	+.00052	-.00031	+.24201	+.00222
4	0.0	0.0	-.00168	-.00827	-.00451	+.01289	+.07547	-.00000	+.03732	+.24871	-.00724
5	0.0	0.0	+.69620	+.00055	+.00001	+1.10146	+.00137	.00000	+.45533	-.07523	-.00320
6	-.36220	0.0	-.46312	-.00014	+.00006	+.01710	+.00114	-.00005	-.01613	-.07696	-.00120
7	-.00073	0.0	+.00336	-.10235	-.01093	+.03279	+.25903	-.00371	-.00548	+.39060	+.00612
8	0.0	+.01486	+.00437	-.12604	+.03924	+.11219	-.00415	+.24634	-.00062	+.24634	+.00291
9	+.00582	0.0	-.22132	-.00069	-.00002	-.56026	-.00114	-.00031	-.13445	-.10524	+.00500
10	0.0	0.0	+.00336	-.09119	+.00095	-.02550	-.13567	-.01102	-.12117	+.14741	-.00755
11	0.0	0.0	+.00235	+.23335	+.00879	-.08800	-.34477	+.00696	-.00289	-.40203	-.00537
12	0.0	0.0	-.72374	+.00152	+.00010	+.14326	+.00160	-.00037	-.04012	-.14386	-.00215
13	+.34587	0.0	+.20218	+.00095	+.00002	+.00813	-.00251	+.00001	+.00476	-.12573	-.00090
14	-.00010	0.0	+.00134	-.20042	+.01030	-.02242	+.04560	-.00703	+.00165	+.63931	+.00403
15	0.0	-.01601	-.00301	+.09505	+.00296	-.05886	-.07251	-.00093	+.00093	+.26290	+.00043
16	0.0	-.00004	-.00235	+.08678	+.00197	+.06278	+.05085	+.01115	+.07692	-.08514	+.00699
17	0.0	0.0	-.50573	-.00041	-.00001	-.15527	+.00182	+.00032	-.07692	-.11312	+.00694
18	-.04158	0.0	+.92860	-.00165	-.00007	-.18021	+.00046	+.00006	+.03133	+.27738	+.00238
19	0.0	0.0	+.00739	+.17852	+.00828	-.08885	-.28890	+.00791	+.02461	-.44421	-.00375
20	0.0	0.0	-.00067	+.00317	-.01244	+.01710	+.07183	+.00429	-.00155	-.47653	-.00162
21	0.0	0.0	+.53600	+.00023	-.00002	-.15499	-.00524	+.00002	+.00393	-.13840	-.00069
22	-.44349	0.0	+.00537	-.00055	-.00005	-.16956	-.00205	+.00002	-.00962	-.00670	+.00032
23	+.00042	0.0	-.00437	+.40760	-.00337	-.03055	-.13395	+.00266	-.00114	+.06937	-.00156
24	0.0	-.00227	-.00470	-.17894	-.00215	-.04230	-.04127	+.00233	+.00031	-.01734	-.00103
25	0.0	0.0	+.04030	+.00041	+.00001	+.09165	-.00479	-.00005	+.02523	-.26999	-.00947
26	0.0	0.0	-.00403	+.00758	+.00001	+.17657	+.20545	+.00555	+.03577	+.22821	+.00649
27	0.0	+.00003	-.00369	-.09298	-.00265	+.10230	+.20887	-.00356	-.01995	+.50451	+.00225
28	0.0	0.0	+.59947	-.00055	-.00002	+.02831	+.00388	+.00005	+.01737	+.47495	+.00212
29	+.00229	0.0	-.87386	+.00124	+.00006	+.44479	+.00684	-.00001	-.00258	+.16712	+.00006
30	0.0	0.0	-.03358	-.14106	-.01005	-.01570	+.13932	+.00112	-.00517	-.28063	-.00001
31	0.0	0.0	+.00067	-.29286	+.00917	-.03559	+.05906	-.00439	+.00289	+.14111	+.00224
32	0.0	0.0	-.05609	-.00124	-.00005	-.28896	-.00251	-.00001	-.00755	+.07962	+.00095
33	+.42201	0.0	+.01981	0.0	+.00003	+.02775	+.00068	-.00005	-.00455	+.12770	+.00059
34	0.0	0.0	+.00134	-.24561	-.00110	+.20067	+.16007	+.00354	-.00227	-.55851	-.00294
35	0.0	-.01344	+.00202	-.15772	+.00182	+.08100	+.07707	+.00074	-.00041	-.20102	-.00082
36	0.0	+.01559	+.00202	+.19891	-.00117	+.06774	+.01482	-.00027	-.00041	-.12258	-.00027

Table 4. Root-Mean-Square Error of the Best Fit Polynomial to the Nodal Displacements of the Mirror In terms of Wavelength for Load Case 1 through 11

No of Terms	1	2	3	4	5	6	7	8	9	10	11
0	.2412	.0099	.7086	.2369	.0083	.7595	.3945	.0111	.2771	.7607	.0145
2	.2339	.0099	.6952	.2369	.0080	.7343	.3808	.0105	.2388	.7607	.0136
3	.2339	.0088	.6952	.2259	.0078	.7343	.3580	.0105	.2388	.7213	.0135
8	.2100	.0064	.6112	.2025	.0069	.5718	.3352	.0097	.1055	.6661	.0120
15	.1767	.0043	.5676	.1763	.0057	.5409	.2964	.0088	.0468	.5794	.0105
24	.1227	.0028	.5105	.1295	.0044	.5269	.2668	.0079	.0238	.4966	.0089
36	.0884	.0000	.4332	.0937	.0032	.5017	.2371	.0071	.0124	.3902	.0072

components of the dominant polynomials (maximum is eighth-order) with respect to the order of the dominant pure radial polynomials of the second load case (maximum is twelfth-order).

The representation of the unsymmetric deflections of load cases No. 3 through No. 11 with the Zernike polynomials show an even greater diversion from the cubic spline fit results than does the asymmetric deflection of load case No. 1. All 36 polynomial coefficients are used for these approximations. Although no set of terms clearly dominate, the ones that have the largest magnitude usually have angular terms with θ for an argument. Figure 34 illustrates this problem with a looped fringe just below the center of the plot. The reason for this, as illustrated in Table 3, is that the radially symmetric properties of the polynomials are not intrinsic to the representation of these unsymmetric deflections. Complete sets of very high order polynomials would be required. A shift of coordinate axes to the actuating point will not alleviate the problem since the Zernike polynomials would no longer be orthogonal within the unit circle.

The finite element analysis also provided slope information with the normal deflection data. The complete set of Zernike polynomials could be differentiated to obtain another complete set of orthogonal polynomials so that the coefficients of an even higher order set could be more accurately solved for. The cubic spline fit is the most accurate representation since both normal deflection and slope information are used in a local interpolation within the finite elements. Therefore, due to the "smoothing" characteristics of a global polynomial fit coupled with the intrinsic properties of the Zernike polynomial, the approximations described above are not accurate in representing the localized deflections of the mirror.

47

THE MECHANICAL DESIGN OF THE DEMONSTRATION MODEL

A 60-cm aperture f/1.5 active mirror was designed to demonstrate the figure control efficiency of the 41-actuator support concept. This system was designed to show the localization of both the position and slope controls. Other advantages such as low mass and structural efficiency could not be practically demonstrated in a model of this size within budget.

The geometric configuration of the model is the same as that used in the finite element analysis, previously described. Three of the actuators were implemented with active components, the remaining 38 were preset mechanically in each of their three degrees of freedom.

An active component is located at each different radial position outside the central actuator. Each degree of freedom is controlled independently by a single servomotor. The remaining manual actuators were positioned before the mirror surface was bonded to the structure. The reference plate was then supported at four symmetrically located points as were used in the finite element analysis program.

Reference Plate

The reference plate consists of a 19.05-mm thick aluminum plate with the appropriate cutouts being made in order to duplicate the configuration used in analysis. It was machined from a solid plate to guarantee a simple homogeneous structure. The cutouts were machined so that each spoke in the reference plate had a 19.05-mm square section. For an actual lightweight system the stiffness and weight of the plate are much too large. Since it will not be used in a study of the intrinsic properties of the support

system's geometric configuration, it is an adequate representation. Three

spokes corresponding to the horizontal element of the three active actuator

trusses were cut out so that removable spokes, with the servomechanisms

attached to them, could be fastened to the reference plate as illustrated in

Fig. 41. The effect of the removable spokes upon the stiffness of the plate

is minimal, since the active actuator posts are not within proximity of each

other. Figure 42 shows an active actuator, located 12.2 cm from the center,

with the removable spoke barely visible inside the servomechanism. For mechan-

ical simplicity, the 0.81 mm diameter steel wire that represents the truss

elements in the support structure, is not attached directly to the reference

plate. Instead, it is sharply bent by the pretension in the truss when passing

through holes in the plate.

In order to duplicate the boundary conditions enforced upon the finite

element model, four countersunk holes were drilled in exact 90° intervals

in those corners of the reference plate corresponding to the four simply

supported nodes of the model. The plate was then supported by four cone-

tipped screws, also located in exact 90° intervals in the test mount. The

completely assembled prototype mounted in the test mount is shown in Fig. 43.

Inactive Actuator

The inactive actuator, as illustrated in Fig. 44, is composed of four

basic components: the 6.8-mm-diameter aluminum actuator post, the 16-mm-

diameter aluminum mirror end cap, the 12.7-mm-diameter reload end cap, and

the 0.8-mm-diameter steel wire that represents the four truss elements in
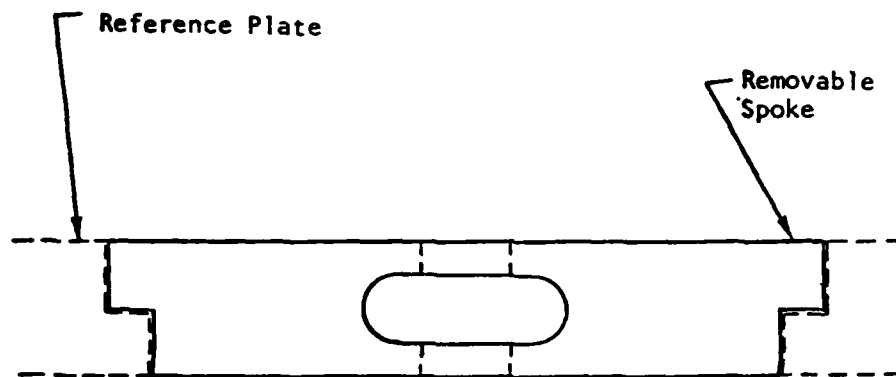
the truss system.
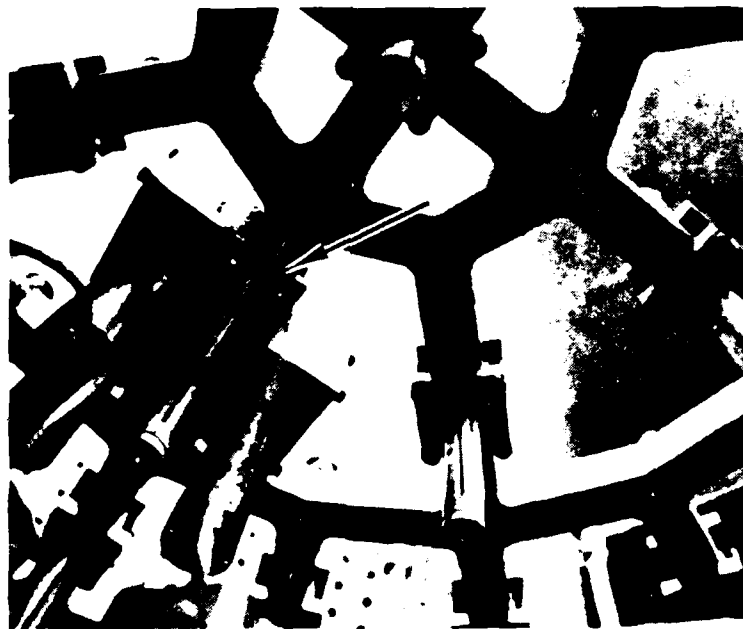
Fig. 41. Remcvable spoke of reference plate.

Fig. 42. The removable spoke of the 12.2-cm active
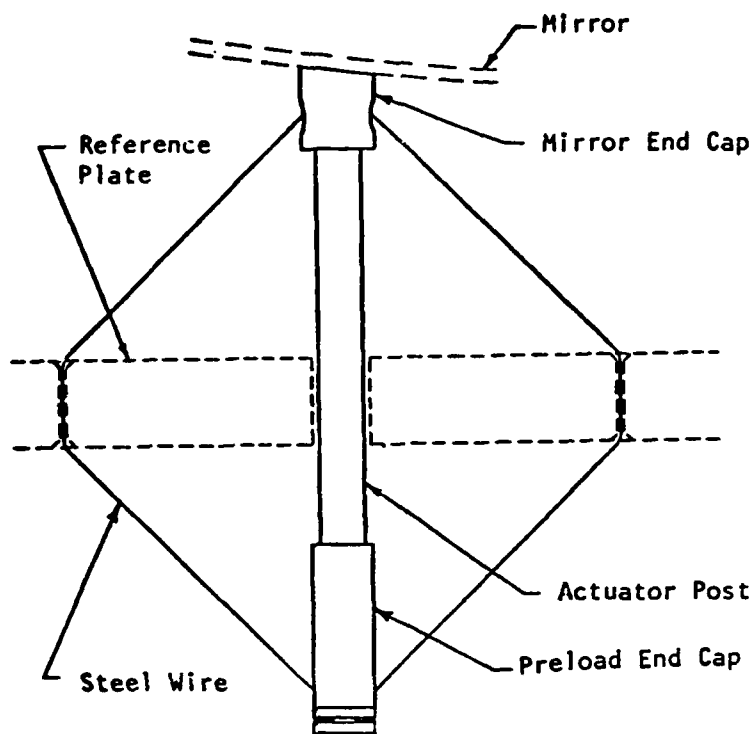actuator mounted to the reference plate.

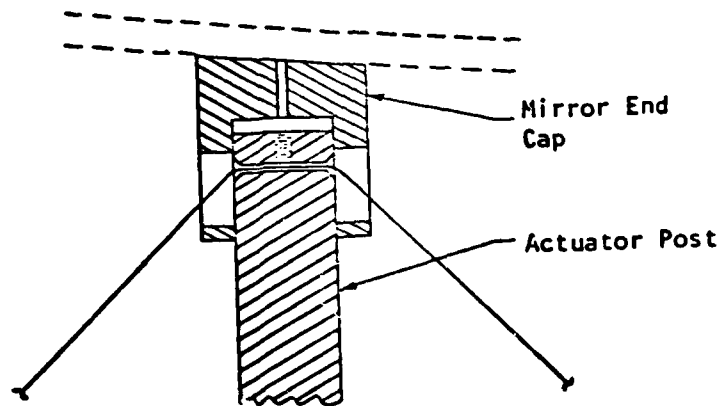Fig. 43. Inactive actuator configuration.

Fig. 44. Mirror end cap.

The mirror end cap provides a rough adjustment in the height of the pre-tensioned actuator to insure contact with the mirror's convex surface before bonding. Figure 45 displays a cross-sectional view of this end cap with the actuator post and steel wire. It can be seen in this figure that a single wire is used for each actuator with the ends fastened to the preload end cap.

Position control of the mirror's surface is made by changing the length of the actuator post with a small variation in the preload of the truss. Tangential and radial slope control is achieved by controlling the position of the actuator post's midpoint. Figure 45 shows two horeshoe-shaped plates with set screws clamped onto the reference plate to provide this control.

Active Actuator

The active actuator, as illustrated in Fig. 46, is composed of five basic components: the 6.8-mm-diameter aluminum actuator post, the 4.75-mm-diameter aluminum normal position control slide with a 16-mm-diameter head, the servo-mechanism, the 0.8-mm steel wire, and the preload end cap which is the same as those of the inactive actuators.

Since the ends of the wire are bent 45° and clamped at the mirror's end of the truss, two steel wires are used. Figure 47 shows this and the normal position control slide in place within the actuator post. A mirror end cap similar to that of the inactive actuator post was not used on the slide, since the three active actuator posts are kinematic reference points for the mirror's position. Normal position control of the mirror's deflection is obtained by inserting an eccentric arm from an output shaft of the servomechanism into the groove at the bottom of the slide. A spring is located between
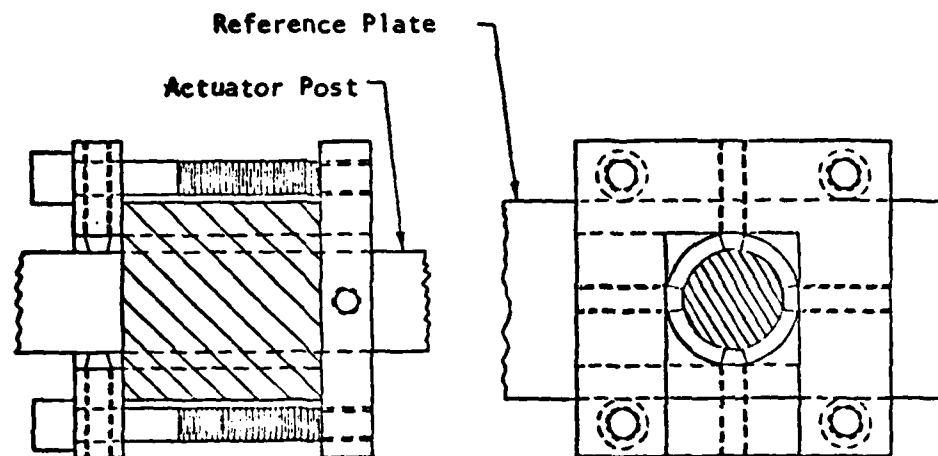
52

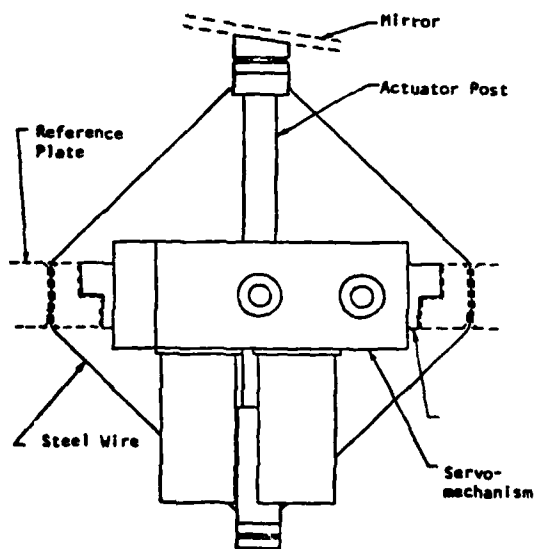Fig. 45.   Slope control of inactive actuators.

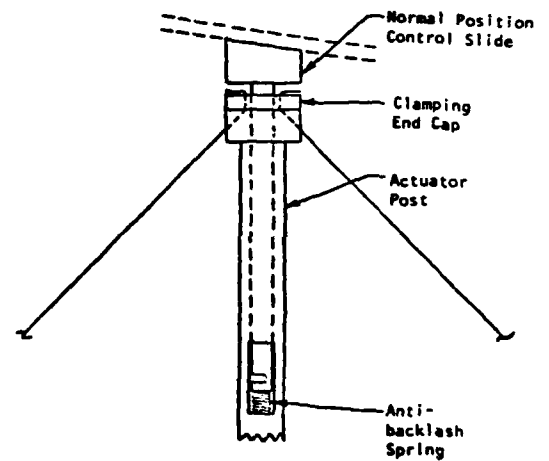Fig. 46.   Active actuator configuration.

Fig. 47.   Normal position control
slide and the actuator
post.

53

the actuator post and the slide to eliminate backlash between the slide and the eccentric arm. The preload in the spring is several times larger than the force necessary to produce the magnitude of deflection desired for the studies.

The servomechanism is a movable gear box having three servomotors, each independently controlling one of the degrees of freedom of the actuator through a single output shaft. Figures 48 and 49 show how the actuator's three degrees of freedom are independently controlled. Slope control in general is obtained by positioning the midpoint of the actuator post. The motion of the transverse slide, which make contact with the post at its midpoint and passes through a clearance slot in the removable spoke, produces the out-of-plane slope control by means of a screw drive. The motion of the entire servomechanism along the spoke controls the in-plane slope of the mirror and is produced by an eccentric arm that engages a slot in the spoke. Teflon pads provide bearing surfaces in the servomechanism for this motion. The normal position control output shaft passes through a clearance hole in the transverse slide. Figure 49 shows the 50:1 worm gear drives between the servomotor and the output shafts for normal position control on the left and in-plane slope control on the right. These two worm gears were machined into sectors because of the reference plate space limitations. A full gear is used in the transverse slides drive since there are no space limitations on this portion of the servomechanism and the linearity of the motion is not dependent upon the angular position of the output shaft.

A fully active operational system may use actuating devices of a completely different configuration than the ones used for this model. In-plane slope control and normal position control may actually be produced by the variation of
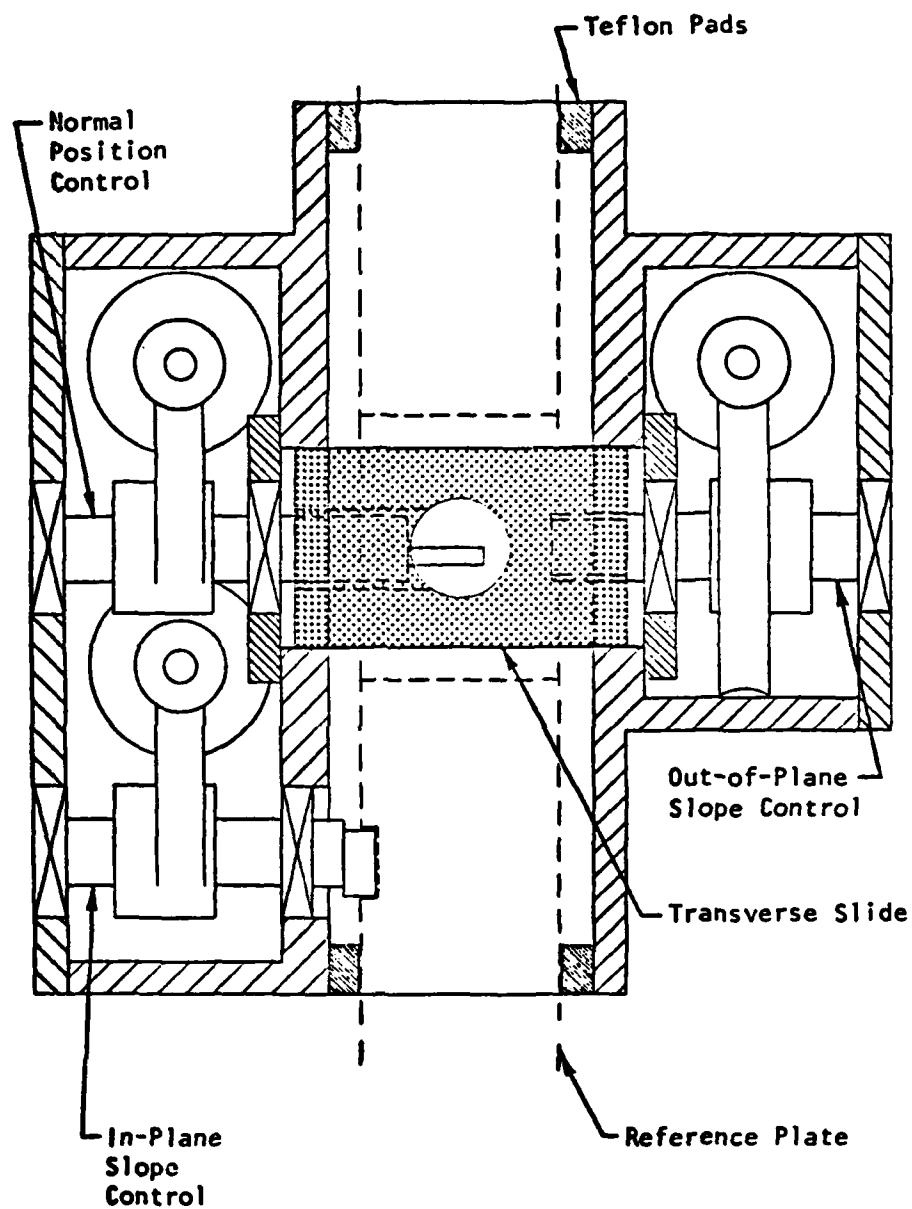
54

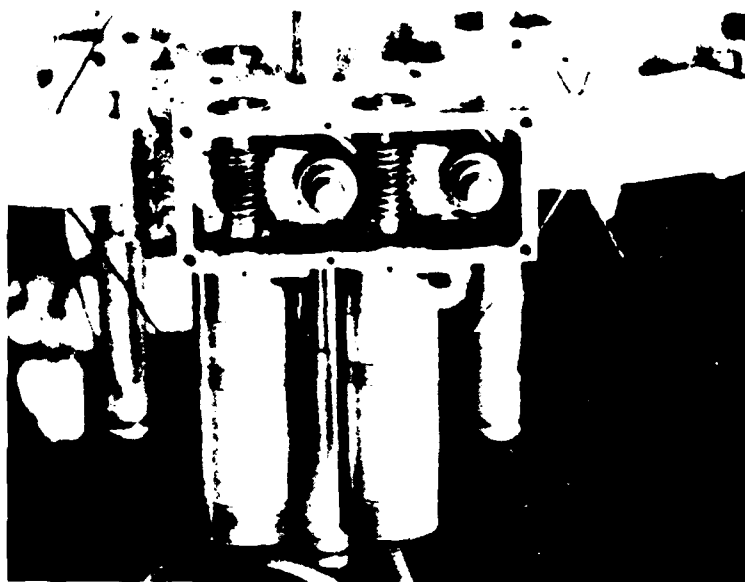Fig. 48. Methods of actuation in the servomechanism.

Fig. 49. Worm gear drives in the servomechanism.

the tension of the lower two truss elements. The two actuators that control this tension would be coupled. If the in-plane slope of the mirror is controlled by the actuator's midpoint, a bending joint would be used at this point so as to remove the bending stiffness of the actuator in this direction and thus minimize the actuating force. The stability of the post would be maintained through the position control of this point.

Thin Shell Mirror

The fabrication of the 60 cm diameter mirror was a delicate process since its thickness is only 5.0 mm. The convex side was generated first from a 40 mm-thick fine-annealed pyrex blank. This surface was then ground into contact with a 40 mm-thick tool with a radius of curvature of 1.83 m, which would later be the support for the mirror when its front surface was processed. Successively finer grits of grinding compound were used to remove any local strains introduced by the surface generator and coarse grinding. With the convex side of the mirror blank bonded with beeswax to the tool, the concave surface was then generated, ground, and polished to a 1.83 m radius of curvature.

To minimize the warping of the plate due to stress in the wax, the wax was only applied to the grooves of the grinding tool, which were spaced on 5 cm centers. A considerable amount of "print-through" resulted from the wax. Areas between the grooves were free to flex slightly due to the small clearance between the tool and the mirror. As a result the surface exhibited irregularities which corresponded to the spacing of the grooves in the grinding tool. A 6 cm diameter aluminum disk was attached to the back of the mirror with pitch. The mirror was then polished on top of the lap, relieving

the pressure caused by the weight of the polishing lap.

Two scatterplate interferograms of the mirror are shown in Fig. 50, where the mirror is supported at two points along its edge, i.e., in a stressed state. The surface quality was still good enough to yield an interferogram over the entire surface of the mirror.

Several problems appeared as the mirror substrate was bonded to the support. Even though great care was taken to use a low shrinkage aluminum-filled epoxy, the deformations caused by the shrinkage are quite apparent in the Foucault test shown in Fig. 51.

The presence of "craters" around the actuators in this figure indicates that the shrinkage of the epoxy is significant. This effect may be due to the discrepancy between the radius of curvature of the convex surface of the mirror and the flat interface surface of the actuator posts. Any residual epoxy outside the actuator posts could also have contributed to this effect. The shrinkage of the epoxy also caused broader deformations in this very flexible mirror due to variations in the thickness of the bonds between the various actuators.

The use of epoxy to bond the pyrex mirror to the support structure yielded some undesirable results. The bond between the epoxy and the actuator posts started to separate but stopped before the components completely debonded. This created stress concentrations in the glass, which has a small tensile strength, and produced a chip from the back side and a total fracture at another actuator point. The cause for this separation is probably due to the incomplete cleansing of the surfaces. An optical cement may be a better choice for a bonding agent. The use of beeswax or pitch would not be practical,

Fig. 50. Scatterplate interferograms of mirror before it was mounted to the assembled support structure.

Fig. 51. Foucault test of mirror after it was mounted to the assembled support structure.

owing to the creep deformations that would occur in these materials. Even with a good bond, shear stresses will be introduced into the glass with thermal deformations because of the difference in the thermal coefficients of expansion between the aluminum actuator post and the pyrex mirror.

An aluminum mirror replaced the damaged pyrex shell. Having approximately equal compressive and tensile strengths, the 5.0-mm mirror can be bonded with epoxy without any probability of fracture.

With the damage to the pyrex mirror late in the project, the goals were modified. The use of the aluminum substrate along with the difficulty experienced in the positioning of the static support points caused the use of holographic interferometry for demonstration on the control of the active support points.

HOLOGRAPHIC INTERFEROMETRY OF THE MODEL

Experimental Procedure

The experimental arrangement is shown schematically in Fig. 52. Argon laser light was passed through a mechanical shutter to a variable density beam-splitter where it was divided into reference and object illumination beams that were separately expanded and spatially filtered. The reference beam was approximately collimated to about a 7.5-cm-diameter at the hologram plane at an incident angle of approximately 20°. The object beam expander/filter was positioned near the center of curvature of the mirror under test slightly inside and to the right. Placing the hologram plane slightly outside and to the left of the center of curvature meant that most of the light reaching the hologram was specularly reflected off the ground surface of the mirror, thus providing the maximum possible object beam irradiance. A 40X microscope objective was necessary to adequately diverge the light so that it overfilled the mirror aperture by some 10%. Considerable care in centering the diverger objective and 12-μm pinhole spatial filter was needed to provide sufficiently uniform illumination so that the entire mirror pupil could be seen in the interferogram photographs. The camera (4 x 5 Crown Graphic with a Polaroid back) used for the latter was tripod-mounted about 7.5 cm behind the hologram plane. This close distance was necessary because the hologram aperture, de-fined by the reference beam diameter, serves as an exit window for viewing the mirror aperture. It would have been preferable to position the camera further back because of depth-of-focus considerations, i.e., the plane of localization of the interference fringes was not the same as the mirror pupil plane. This will be discussed later in more detail.
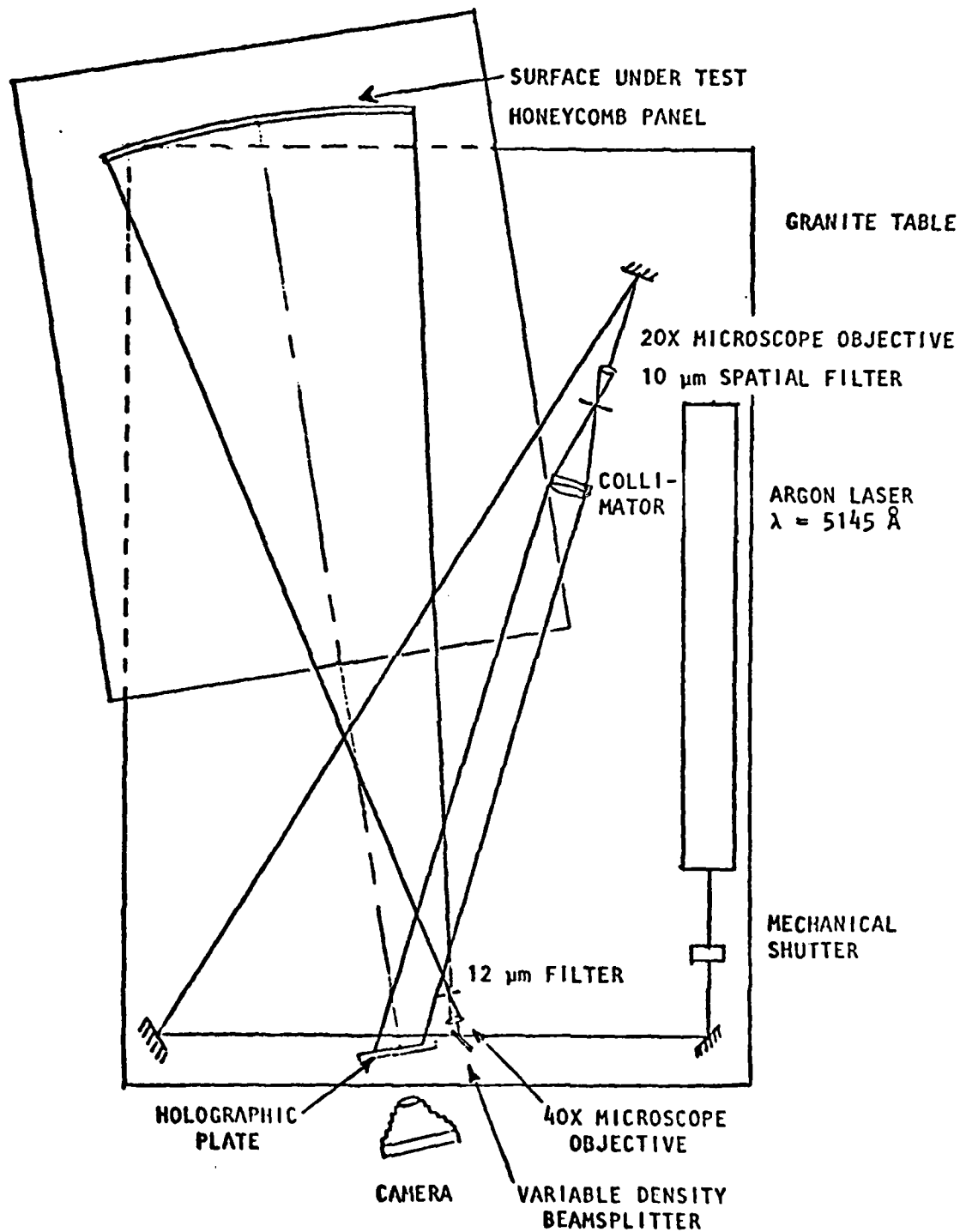
Fig. 52. Schematic layout of holographic interferometric test of 60-cm active mirror model.

The hologram plate holder was demountable in a kinematic support so that the plate could be accurately repositioned in the same location after processing. Micrometer screw adjustments for transverse displacements of the hologram provided capability for introducing "tilt" fringes in both directions.

Agfa 10E56 4 x 5 inch holographic plates were used to make the holograms, which were bleached after development for increased diffraction efficiency. The object/reference beam ratio was approximately 6:1. For this beam ratio the optimum total exposure was found to be 15 to 20 ergs/cm^2 followed by development in full strength D-19 for 5 min at 68°F and bleaching in EB-2 solution for approximately 1 min. The argon laser, a Spectra Physics Model 165, was operated single-wavelength at $\lambda = 0.5145$ Å, which is the wavelength of maximum sensitivity for the 10E56 emulsion, and in a single longitudinal mode by means of an intracavity etalon to provide sufficient coherence length so that optical path matching was not required. This was at the cost of reducing the available power from the laser to approximately 100 mW. However, it was possible to obtain the desired exposure level of 15 to 20 ergs/cm^2 with an exposure time of 1/8 sec, which kept fringe visibility reduction due to vibration and air turbulence within reasonable bounds. Indeed, the major cause of reduced visibility was the limited depth of focus already mentioned.

The whole apparatus was mounted on a 1.8-m x 0.91-m granite table isolated by air-filled rubber inner-tubes, except for the tripod-mounted camera used to photograph the interferograms. The problem of shutter-induced vibrations during the hologram exposures was eliminated by the simple expedient of raising the shutter off the table and hand holding it while operating it. The apparatus, including the support structure for the vertically mounted active mirror, is shown in Fig. 53.
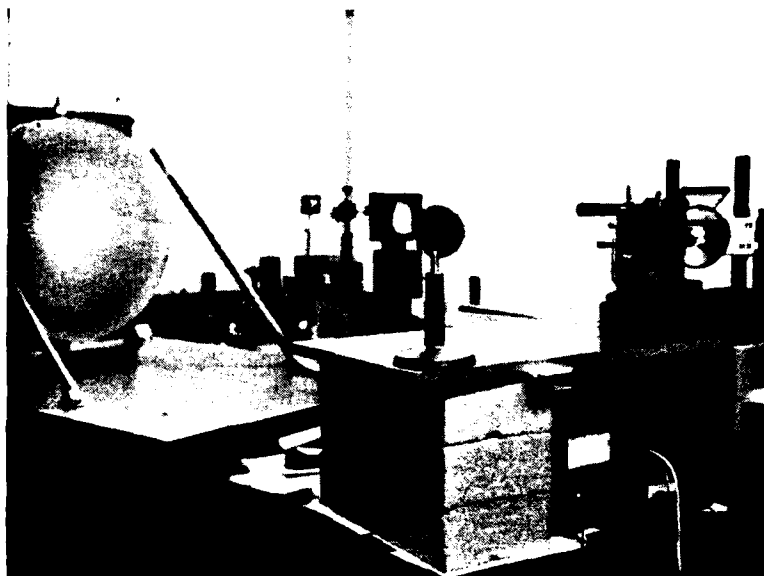
Fig. 53. Photograph of holographic interferometric test of 60-cm active mirror model. (The ground aluminum mirror assembled to give it its active support structure is vertically supported on a honeycomb plate which rests in turn on a 1.8-m x 0.9-m granite table.) The optics for recording and reconstructing the holograms are supported on cinder blocks which also rest on the granite table. The plate holder can be seen in the right foreground, located approximately at the center of curvature of the mirror.

After exposure, processing, and repositioning of the holograms, real-time holographic interferograms were observed visually and photographed, using the same illumination wavelength of 0.5145 µm. Surface deformations were induced by operating the gear motors controlling the z positions and the in-plane radial and tangential slopes of the three active actuators. The remaining 38 passive posts were clamped to the reference plate. The mirror support structure and actuator drives have been fully described.

The interferograms were photographed on Type 57 Polaroid High Speed Film (ASA 3000) at very high f/numbers and correspondingly long exposure times, typically f/32 at 1/10 to 1/2 sec. This was for the purpose of making the depth of focus as large as possible since the fringe localization plane was in general far removed from the mirror pupil plane, as previously mentioned-- usually quite close to the camera lens, e.g., 2.5 or 5 cm--whereas the mirror pupil was more than 18 cm away. This is a troublesome and fairly common difficulty in holographic interferometry of diffusely illuminated subjects. It can also lead to errors in interpretation of the fringes as contours of equal surface height deformation. In this work we have not taken such possible errors into account, primarily because the analysis is complicated to the point where lack of time precluded it, but also because other errors dominate, e.g., due to fabrication and assembly imperfections in the actuator structure causing position backlash or inadvertent slope errors or fringe errors due to air turbulence.

65

RESULTS

An initial series of interferograms was made without the introduction
of tilt. Unfortunately, the series was not complete--only the 0.4 zone
actuator modes and one of the edge actuator modes were photographed--since
the intention was to analyze the fringe data with the help of the computer
program FRINGE. Accordingly, tilt was introduced in all the later inter-
ferograms to give open fringes, which are easier to scan than closed fringes
using the present manually operated comparator. A complete series of inter-
ferograms with tilt for all three modes of all three actuators was made.
These results are presented in the following.

Figure 54 shows the effect of a tangential slope change produced at the
0.4 zone (9.5-cm radius). It bears a good resemblance to the prediction of
the computer model (see Fig. 21). The fringe contour shapes appear very
similar but more localized than predicted, as discussed below. Several fringes
due to over-all curvature change can be seen. This was caused by a change of one
or two degrees Fahrenheit in the room temperature between the time the holo-
gram was exposed and the time the interferogram was made. Some tilt is also
noticeable, as well as irregularities due to air turbulence and reactions
between the deformed shell and the fixed, passive actuators.

The deformation produced by a radial slope change also at the 0.4 zone
is shown in Fig. 55, the result of a small z-displacement is shown in Fig. 56,
and a large z-displacement is shown in Fig. 57. Again, the fringe shapes are
more or less as predicted (compare Figs. 22 and 23), but are more localized.
The reactions of the passive actuators are clearly seen in Fig. 57. It should
be noted that the peak occurring at about three o'clock at the 0.5 zone is

Fig. 54.   Tangential slope change, 0.4 zone.

Fig. 55.   Radial slope change, 0.4 zone.

67

Fig. 56. z displacement, 0.4 zone (no tilt).

Fig. 57. z displacement, 0.4 zone (28 fringes).

68

not an actuator reaction, but an artifact introduced by the experimenter while demonstrating the real-time nature of the holographic interferometry-- finger pressure on the back of the shell, estimated at 5 to 10 lbs., apparently produced a permanent deformation in the form of a dimple. It was subsequently removed by making a new hologram.

Surface profiles along the axes of symmetry in the directions of the slope changes were computed by hand for the tangential slope change mode of Fig. 54 and for the radial slope change mode of Fig. 55 at the 0.4 zone. These profiles are plotted in Figs. 58 and 59 along with the corresponding computer predictions. The shapes are similar, however, the peak-to-valley separation in the experimental profiles is less than predicted--particularly in the case of the tangential slope change. Thus, the deformations appear to be more localized than predicted, as already noted.

Figure 60 shows the effect of tangential slope change of the edge actuator. Agreement with the computer prediction (Fig. 27) is not as good as in the previous cases--the experimentally observed deformation is much more localized, and bi-lateral symmetry is observed. The latter, suprisingly, is absent in the computer result. The possibility of the computer prediction being in error has been raised, but not examined further to date. Also evident in Fig. 60 are more art-ifacts due either to incomplete removal of previous actuator displacements or to permanent creep due to these displacements. One fringe of z-displacement for the 0.85 zone actuator (approximately 10 o'clock) and about one fringe of mostly radial slope change at the 0.4 zone actuator (6 o'clock) can be observed.

The following series of interferograms shown in Fig. 61 were made with tilt introduced by vertical displacement of the hologram during reconstruction
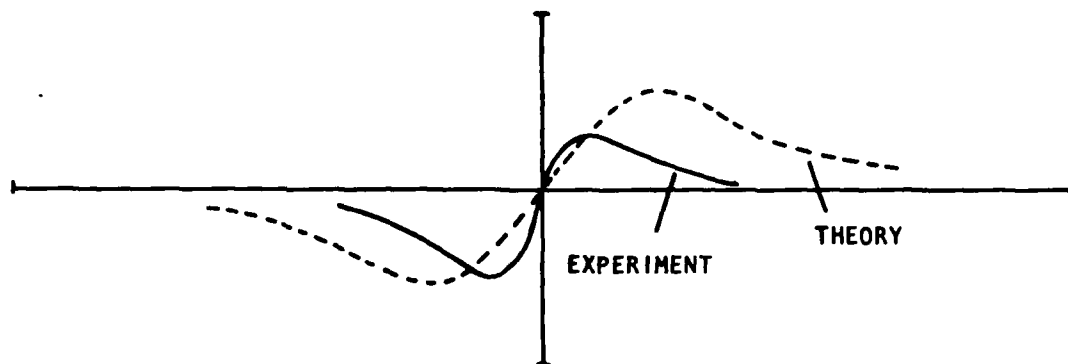
Fig. 58. Surface profile through axis of symmetry, tangential slope change, 0.4 zone.
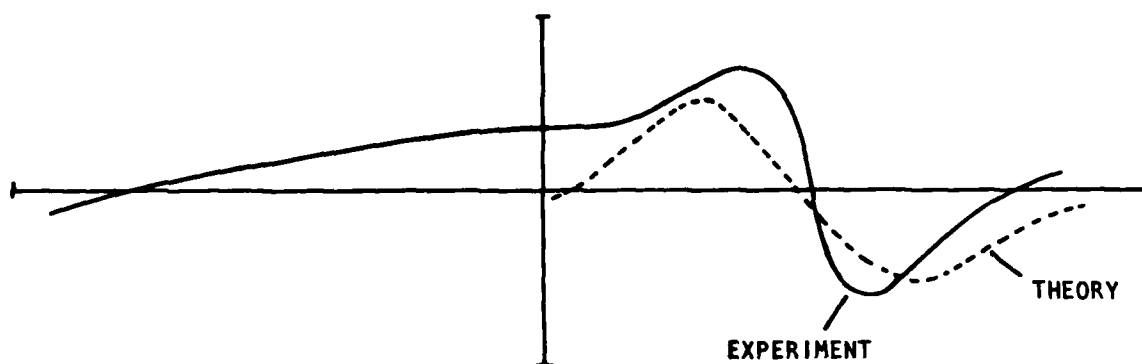

Fig. 59. Surface profile through axis of symmetry, radial slope change, 0.4 zone.

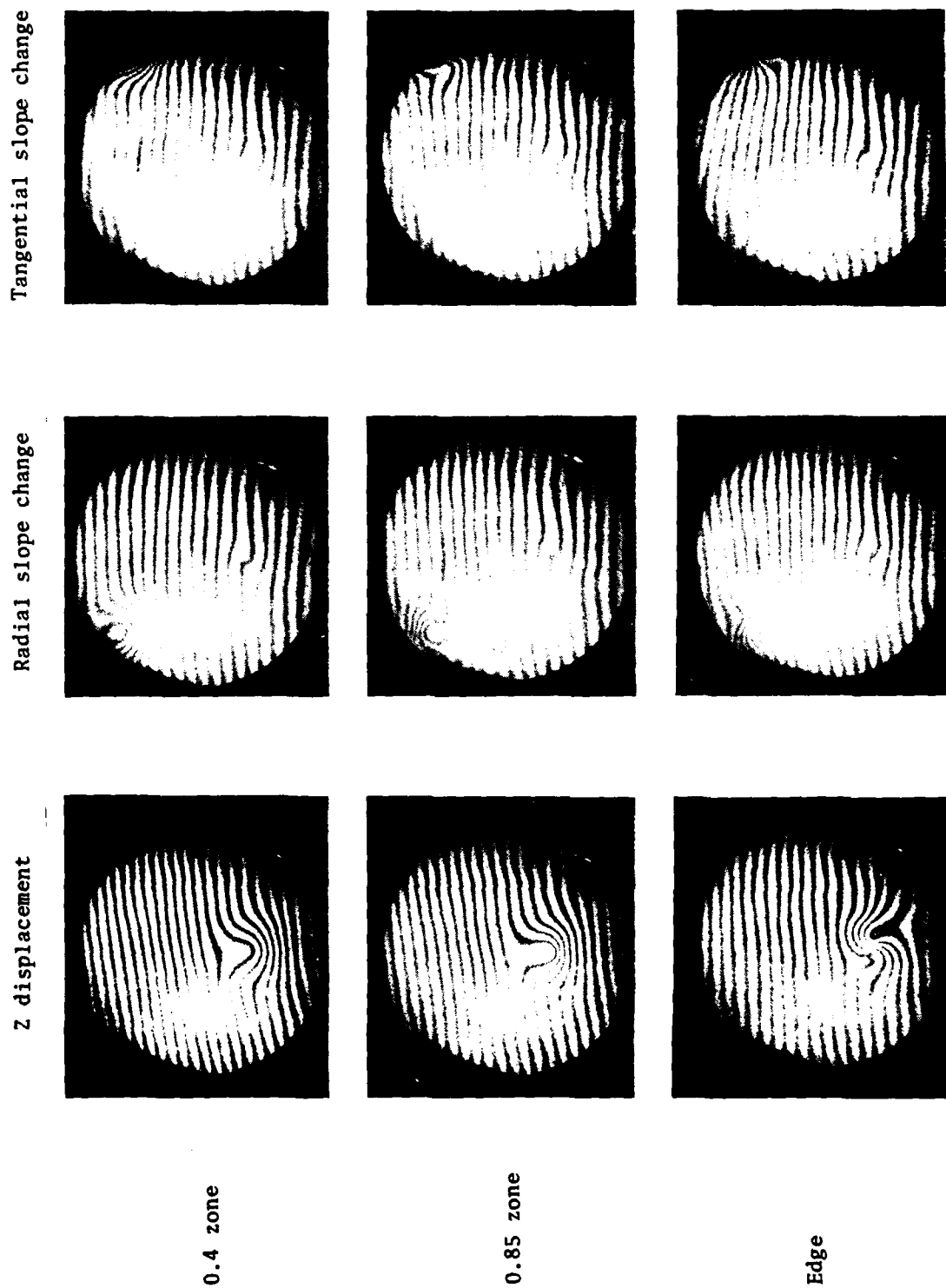Fig. 60. Tangential slope change, edge.

Fig. 61. Interferograms showing z displacement, radial slope change, and tangential slope change at 0.4 zone, 0.85 zone, and edge.

Tangential slope change

Radial slope change

z displacement

0.4 zone

0.85 zone

Edge

72

to expedite the input of the interferometric data to the FRINGE program, as previously indicated. Unfortunately, because of the tilt it is more difficult to make a direct visual comparison between these interferograms and the predictions of the computer model. It is possible to remove tilt and defocus using FRINGE and plot the residual errors by a linear interpolation method. Five interferograms have been scanned and analyzed, and the results of four are shown in Fig. 62. (The FRINGE program also has the capability of fitting a Zernike polynomial expansion to the surface represented by the interferometric data and extracting aberration information in addition to overall tilt and defocus, but this feature was not found very useful because the extreme localized nature of the deformations cannot adequately be represented by the limited number of terms (36) in the expansion presently available in the program.) Note that the order of presentation differs here from the previous interferograms. They are in the order that the interferograms were made in the laboratory, which consisted of the follwoing sequence: an actuator displacement, a photograph of the resulting interference fringes, removal of the displacement, a second actuator displacement, etc. The significant point here is that the "removal" step was not always complete, as can be seen in the interferograms in the bottom two rows where a residual slope error occurs at the 0.4 zone. Some similar evidence can be found in the FRINGE plots of Fig. 62b.

Figure 62a shows a z-displacement at the 0.4 zone which agrees well with the previous result (Fig. 56). However, the radial slope change example in Fig. 21 appears to have a significant amount of residual z-displacement. If we compare with the corresponding case in Fig. 55, we may recognize some
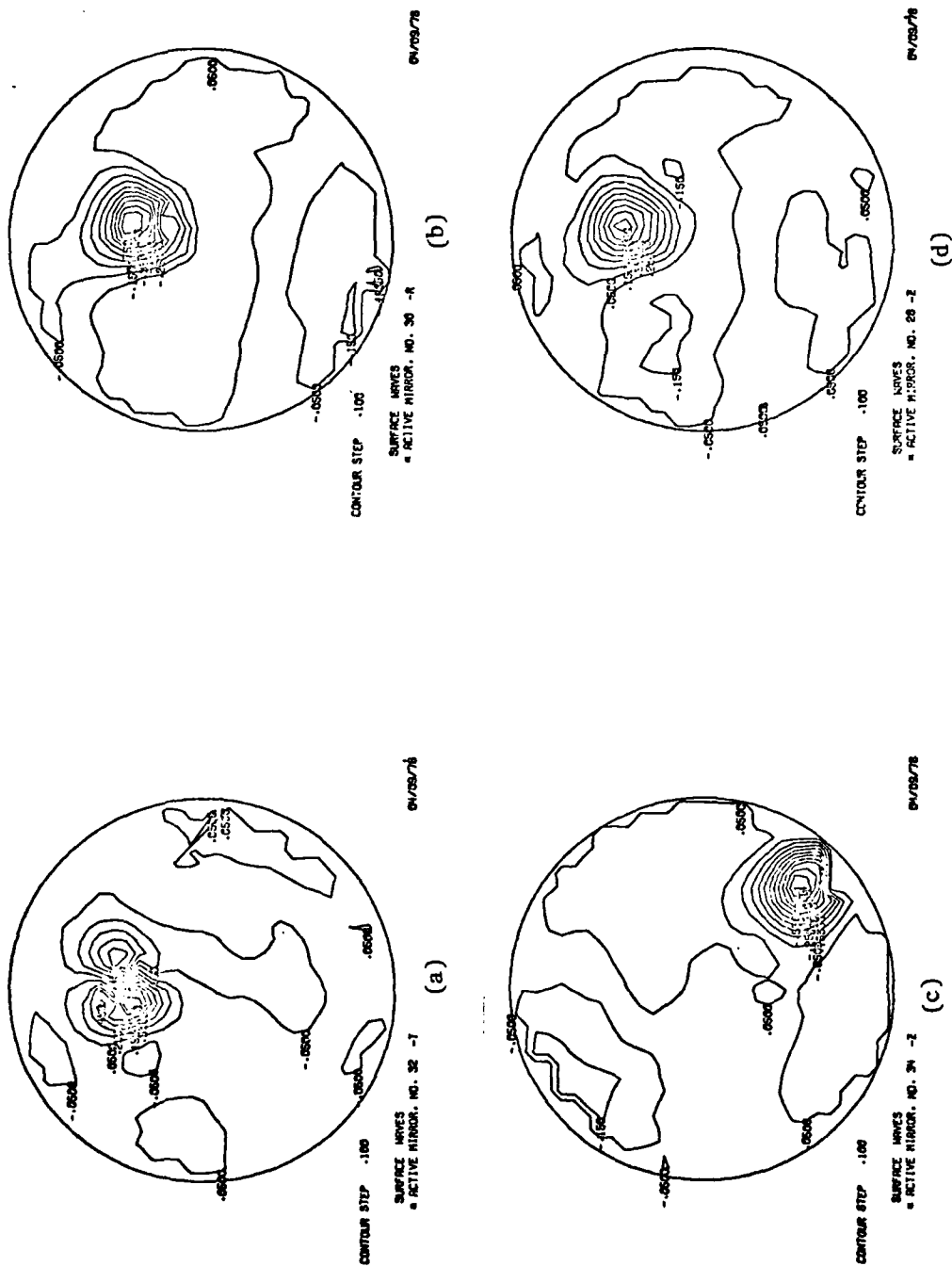
CONTOUR STEP .100

SURFACE WAVES
= ACTIVE MIRROR. NO. 30 -R

04/09/78

(b)

CONTOUR STEP .100

SURFACE WAVES
= ACTIVE MIRROR. NO. 28 -2

04/09/78

(d)

CONTOUR STEP .100

SURFACE WAVES
= ACTIVE MIRROR. NO. 32 -7

04/09/78

(a)

CONTOUR STEP .100

SURFACE WAVES
= ACTIVE MIRROR. NO. 34 -2

04/09/78

(c)

Fig. 62. Plot of residual errors for four interferograms.

74

similarity. But, it seems likely that the actuator performance is question-able in both examples. Note that the outer valley is deeper than the inner hill in Fig. 55, whereas symmetry would be expected. The result of tangential slope change for the 0.4 zone actuator in Fig. 62c is somewhat better, but shows residual radial slope error not completely removed. The corresponding case in Fig. 54 is a better example, appearing to be a pure tangential slope error. Figure 62d, showing a z displacement at the 0.85 zone, has an unexplained component of radial slope error, which mars an otherwise good confirmation of the computer prediction.

It is obvious that a serious oversight was made in neglecting to obtain a complete set of interferograms *without* tilt, as these afford a direct compari-son with theory without the complications of fringe scanning and computer re-moval of tilt which inevitably introduce further errors. We would then have been able to present complete results for all the actuators in clearer fashion.

CONCLUSIONS

The experimental results, though incomplete, support the computer model in a qualitative way, with the exception of the anomalous result for the tangential slope change produced at the edge actuator (Fig. 62d). In that case there is some question about the detailed validity of the computer model prediction.

There is also some discrepancy in the details of the matching between theory and experiment--the experimentally produced deformations are somewhat more localized than predicted. This is to be expected because the computer model was set up for the entire system including the lightweight structure, as mentioned earlier. The stiffer experimental structure would result in more localized results.

The use of the aluminum mirror was not without some additional problems. This shell was cut from a solid 37-mm-thick aluminum plate, rather than from an aluminum forging. As a result, as the curved surfaces were generated into the plate, some warping occurred. The over-all result was a variation in the thickness of the mirror that introduced additional artifacts into the experimental data. As a result, further analysis of the data, although possible, would not increase its reliability.

Within the limitations of the experimental data, the accuracy of the computer model has been demonstrated to the 60 cm aperture.

Figure 63 is a comparison of weight estimates for various mirrors and mirror cell combinations. The solid monolithic mirror estimates are based on a 6:1 diameter-to-thickness ratio and a cell weight equal to the mirror weight.

The lightweight mirror is an extrapolation of the fused silica eggcrates with cell estimated at half the substrate weight, which is close to current space applications. It is estimated that the weight of the substrate is proportional to $D^{2.7}$ where D is the mirror diameter.

The integrated optical structure studied under this contract has been estimated with the same number of actuators throughout. The stiffness which is proportional to the third power of the thickness is maintained to allow a scaling ad $D^{2.4}$. Weight saving in the 3-m region is still a factor of 5 better than that for current optical systems.
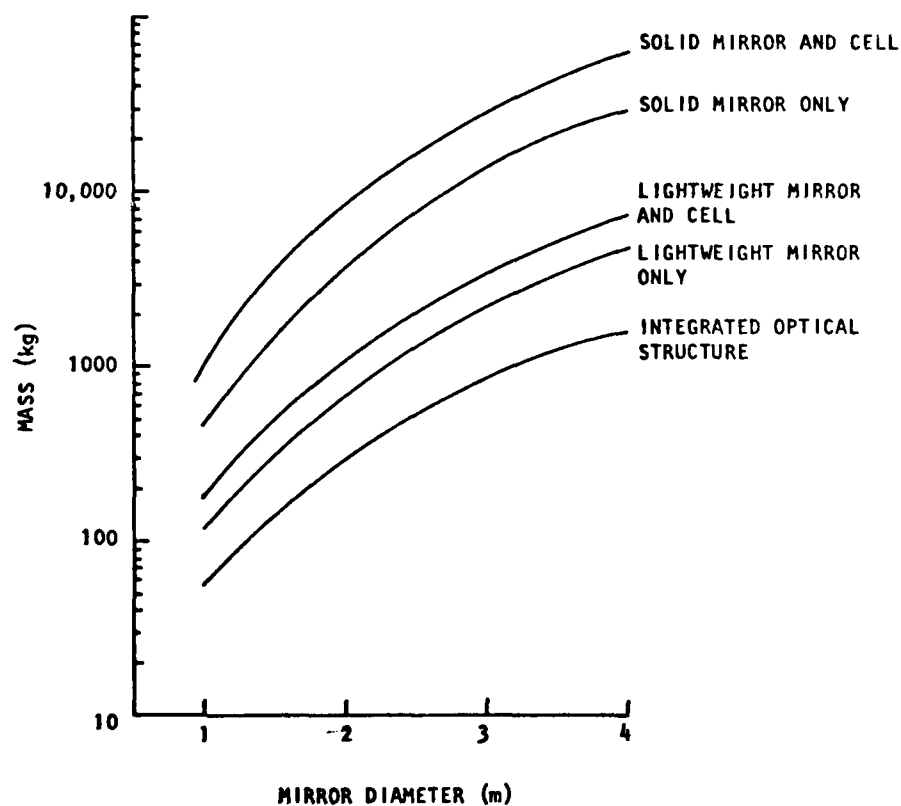

Fig. 63. Comparison of mass estimates for systems.

REFERENCES

Bathe, K. J., E. L. Wilson, and F. E. Peterson, "A structural analysis program for static and dynamic response of linear systems," EERC-75-11, College of Engineering, Berkeley, California, 1973.

Loomis, John S., FRINGE User's Manual, Version 2, Optical Sciences Center, University of Arizona, Tucson, Arizona, November, 1975.

Zienkiewicz, I. C., The Finite Element Method in Engineering Science, McGraw-Hill, New York, 1971.